



Delft University of Technology
Faculty of Civil Engineering and Geosciences
Department of Geosciences and Engineering

**Multilevel Multiscale Method for Embedded
Discrete Fracture Modeling Approach (F-MLMS)**

Thesis submitted to the
Delft Institute of Applied Earth Sciences
in partial fulfillment of the requirements
for the degree

MASTER OF APPLIED EARTH SCIENCES

by

S. Mousa HosseiniMehr
S.HosseiniMehr@student.tudelft.nl

Delft, the Netherlands
23 August 2016

Copyright © 2016 S.Mousa HosseiniMehr. All rights reserved.

DARSim
Delft Advanced Reservoir Simulation

Author

S. Mousa HosseiniMehr
S.HosseiniMehr@student.tudelft.nl

MSc Student, Petroleum Engineering & Geosciences
Department of Geosciences and Engineering
Delft University of Technology

Title

Multilevel Multiscale Method for Embedded Discrete Fracture Modeling (F-MLMS)

Advisors

Dr. Hadi Hajibeygi
H.Hajibeygi@tudelft.nl

Principal Advisor, Assistant Professor
Department of Geoscience and Engineering
Delft University of Technology

Matteo Cusini
M.Cusini@tudelft.nl

Daily Supervisor, PhD Candidate
Department of Geosciences and Engineering
Delft University of Technology

Committee

Prof. Ir. Cor van Kruijsdijk
C.P.J.W.vanKruijsdijk@tudelft.nl

Committee, Professor
Department of Geoscience and Engineering
Delft University of Technology

Prof. Dr. Giovanni Bertotti
G.Bertotti@tudelft.nl

Committee, Professor
Department of Geoscience & Engineering
Delft University of Technology

Dr. Ir. Frans van der Meer
f.p.vanderveer@tudelft.nl

Committee, Assistant Professor
Computational Mechanics
Delft University of Technology

Dr. Alexander Lukyanov
A.Lukyanov@tudelft.nl

Committee
Applied Mathematics
Delft University of Technology

Abstract

Accurate numerical simulations of multiphase flow in fractured porous media require high resolution grids to explicitly capture the effect of fractures on the flow field without using excessively upscaled quantities (e.g., modified rock permeabilities). For field-scale applications, as the consequence of large-scale domains and many explicit fractures, the size of the (non)linear systems becomes out of the scope of the classical numerical methods. Thus, various advanced numerical methods have been introduced to reduce this computational challenge. The Embedded Discrete Fracture Model (EDFM) which employs sets of independent grids for the rock matrix and the fractures (represented as lower dimensional domains). By employing two separate grids, coupled by a transfer function, EDFM allows to avoid adapting the matrix grid to accommodate the presence of fractures. Therefore, computational complexities with respect to the fracture geometries are significantly reduced. Even after employing EDFM, the size of the systems for real-field applications is still too large to be solved accurately with classical solvers. This challenge motivates the development of Multiscale Finite Volume (MSFV) method, which is the focus of this work, as well. The MSFV method efficiently solves the pressure (flow) equations by solving it at a coarser resolution, while honoring the fine-scale heterogeneous data. Recently, an efficient MSFV method for EDFM approach (F-AMS) was developed and tested for many cases of practical interests [1]. Even though the F-AMS was found efficient for many scenarios, its applicability is limited to only the use of 2 levels of grids (fine and coarse). For real-field applications, where there exist several millions (or billions) degrees of freedom, the construction of only 1 level of coarse grid resolution may not be sufficient. Of high interest to the community is the development of a multiscale method which allows for arbitrary number of accurate coarse resolutions. In this work, for the first time in the multiscale community, a novel multilevel multiscale finite volume method for fractured porous media (F-MLMS) is developed. F-MLMS is successfully applied to a set of synthetic 2D test cases and its performance is carefully studied. Employing a multilevel strategy becomes crucial for field-scale applications, where a single level of coarsening is not enough to reduce significantly the size of the linear systems to be solved. The use of two independent grids allows to employ different coarsening strategies for the two media. Consequently, F-MLMS represents an important step forward for the application of multiscale methods to naturally and induced fractured reservoirs, with complex fracture networks.

Acknowledgments

Two years of studying master of science at TU Delft, with numerous unforgettable memories and worthy experiences, is finally over and the completion of my MSc thesis brings this adventure to its end.

I still remember the level of my excitement in September 2014 to start my master studies. I have always been in love with physics and mathematics and somehow I have been more interested in mathematical modelings and computational aspects of fluid dynamics. Attending the course "Rock Fluid Physics" taught by Dr. Hadi Hajibeygi marked a rise in my interest in this criteria. Almost all the lecturers I have encountered were good in knowledge transfer, but Hadi had a great passion to convey the concept of the course especially when he briefly introduced reservoir simulation. Since then, I gain interest and curiosity about simulation even though I had no information about the details. Then I joined Delft Advanced Reservoir Simulation (DARSim) and gained lots of knowledge from insightful meetings and discussion. Hadi's passion and his way of teaching during "Reservoir Simulation" course finalized my decision to choose my master thesis topic. Hadi offered a challenging topic for my master thesis, I accepted and he became my principal advisor. Now it is almost nine months since I started my thesis. During this period, I learned a lot of scientific topics. Beside many interesting and nice moments, I also faced many challenges and difficulties. But I do not regret starting this journey even a bit. Hadi was impressively supportive, helpful, patient and a good motivator. Whenever I had questions and wanted to meet, he was always available and ready even if he was not physically there. Therefore I would like to thank him for all of his support, time and attention he put to help me drive to the end of this journey. It is hard to imagine anyone else be like him.

I would like to thank my daily supervisor Matteo Cusini. He kindly put lots of his time helping and answering my questions. Let me not forget to thank Matei Tene as well. He also put his time to give suggestions and answers to my question. I would also like to thank Professor Cor van Kruijsdijk, Professor Giovanni Bertotti, Dr. Frans van der Meer and Dr. Alexander Lukyanov for being part of my exam committee. With similar importance, I would like to thank other DARSim members (Rafael, Barnaby, Sebastian, Frank, Jakolien, Siavash, Sander and others) for attending my presentation, giving me good mood with fruitful discussions and providing innovative suggestions during the development of this MSc project.

Finally, I am thankful for my parents' financial and moral support. Without their support I could never have the opportunity to continue my studies and gain all the knowledge and experience I have acquired so far.

Mousa HossseiniMehr
22 August 2016, Delft

Contents

Acknowledgments	2
Lists	iii
Figures	iii
1 Introduction	3
1.1 Fracture Modeling Approaches	4
1.2 Discrete Fracture Models (DFM)	4
1.2.1 Conforming Discrete Fracture Model (CDFM)	4
1.2.2 Embedded Discrete Fracture Model (EDFM)	5
1.3 Multiscale Methods	5
1.4 Multilevel Multiscale Approach (MLMS)	5
1.5 Multilevel Multiscale Method for Fractured porous media (F-MLMS)	6
1.6 Research Goals	6
2 Embedded Discrete Fracture Model (EDFM)	7
2.1 Description of Fracture Network	7
2.2 EDFM Formulation	7
2.3 Discretized Form of the Pressure Equation	9
2.3.1 Connectivity Index	10
2.3.2 Fracture Intersection	10
2.3.3 The system of pressure equations	11
2.4 EDFM Results and Verification of the Developed Simulator	12
2.4.1 Test Case 1: Quarter of Five Spot with One Diagonal Fracture	13
2.4.2 Test Case 2: Line drive with Two Fracture Perpendicular to each other, ”+” Shape	13
2.4.3 Test Case 3: Line drive with Two Fracture Perpendicular to each other, ”x” Shape	13
2.4.4 Test Case 4: Series of Intersected Fractures	13
2.5 Discussion	13
3 Multiscale Finite Volume Method for Fractured Porous Media (F-MSFV)	19
3.1 MSFV Grids	19
3.2 F-MSFV Formulation	19
3.3 Basis Functions	21
3.3.1 Algebraic Form of Basis Functions (Prolongation Operator)	25
3.4 Coarse-scale system	25
3.5 Results and Validation	26
3.5.1 Test Case 1: Quarter of Five Spot with no fracture	26
3.5.2 Test Case 2: Quarter of Five Spot with One Diagonal Fracture	26
3.5.3 Test Case 3: Line drive with Two Fractures Perpendicular to each other, ”+” Shape (fractures on the boundaries of primal coarse grids)	26

3.5.4	Test Case 4: Line drive with Two Fractures Perpendicular to each other, ”+” Shape (fractures on the boundaries of dual coarse grids)	27
3.5.5	Test Case 5: Line drive with Two Diagonal Fractures Perpendicular to each other, ”x” Shape	27
3.5.6	Test Case 6: Line drive with 5 Random Fractures	27
3.6	Discussion	27
4	Multilevel Multiscale Method for Embedded Discrete Fracture Model (F-MLMS)	35
4.1	MultiLevel MultiScale Finite Volume Method (MLMS)	35
4.1.1	MLMS Formulation	35
4.1.2	MLMS Coarse Grid Construction	36
4.1.3	MLMS Prolongation and Restriction Operators	36
4.1.4	MLMS Basis Functions	37
4.2	MultiLevel MultiScale Finite Volume Method for Fractured Porous Media” (F-MLMS)	37
4.2.1	F-MLMS Approach	37
4.2.2	F-MLMS Implementation	38
4.2.3	F-MLMS Basis Functions	40
5	MLMS and F-MLMS Results and Discussion	43
5.1	Test Case 1: MLMS Line Drive (Four Spot)	43
5.2	Test Case 2: MLMS Quarter of Five Spot	43
5.3	Test Case 3: F-MLMS Quarter of Five Spot with One Diagonal Fracture	43
5.4	Test Case 4: F-MLMS Line Drive with Two Fractures Perpendicular to each other, ”+” Shape	44
5.5	Test Case 5: F-MLMS Line Drive with 5 Random Fractures Intersecting with Each Other	44
5.6	Test Case 6: Comparison: F-MLMS Line Drive with Two Diagonal Fractures Perpendicular to Each Other, ”x” shape	44
5.7	Discussion and Validation of Results	44
6	Conclusion	53
	Appendices	

Figures

1.1	a) Fracture network in flat-lying carbonates in the Potiguar Basin, Apodi, Rio Grande Do Norte, Brazil. Photo made by K. Bisdom, PhD Candidate, TU Delft [2]. b) Fractures together with inclined layering, Brochterbeck quarry, Germany. Photo taken by the author.	3
1.2	A schematic sample showing the grid construction of different DFM approaches.	4
2.1	Schematic of EDFM concept. The fractured media (a) is independently split into a matrix grid system (b.1) and a fracture network grid (b.2). Also the matrix and fracture grids are showed on top of each other (c) with overlapped matrix cells highlighted with color.	8
2.2	Matrix cell (i, j) with its surrounding cells and fracture elements overlapping the matrix cells in this region. Here, fracture elements $k-1$, k and $k+1$ have penetrated the matrix cell (i, j)	9
2.3	The area fraction calculation for connectivity index for 2 different cases.	10
2.4	Calculation of average distance between fracture element and matrix cell ($\langle d \rangle_{ij,k}$) for different cases.	11
2.5	Intersection between two fractures. The nodes in the figure are the centers of each fracture elements.	11
2.6	IMPES method flowchart.	12
2.7	Results of test case 1: a diagonal fracture having significant effect on the productivity of the reservoir.	14
2.8	Results of test case 2: a cross-shaped fracture being accurately captured through EDFM formulation. Note that due to high conductivity of the fracture network the pressure drop inside fractures is very small, compared with that of the matrix rock.	15
2.9	Results of test case 3: diagonal-shape fracture network being independently discretized along with the matrix grid cell. This test case illustrates the advantage of EDFM over DFM in terms of grid complexity, as no adjustment of matrix grid cells for fractures is necessary in EDFM.	16
2.10	Results of test case 4: a complex fracture network spanning most of the reservoir is being modeled by EDFM. Note the effect of fracture in flow and transport is quite significant, leading to early water break through.	17
3.1	Construction of primal and dual coarse grid structure in multiscale approach for a 2D sample with 15×15 of fine grids. This sample is divided into 3×3 primal coarse grids. The coarsening ratio here is 5.	20
3.2	Construction of primal and dual coarse grids for fracture. In this example, fracture has 21 elements and is divided into 5 unequal primal coarse grids. The coarsening ratio here is 5.	20
3.3	Construction of coarse grids for 2D fractured media. Coarsening ratio is 9.	21
3.4	Local basis function (without any fracture) for the coarse node $(3, 2)$ in 2D (left) and 3D (right) view, for a heterogeneous test case. The white lines are the boundaries of primal coarse grids.	22
3.5	A matrix basis function for the sample shown in figure 3.3.	22

3.6 Fracture basis functions at first and last coarse nodes of one fracture for the sample shown in figure 3.3. 23

3.7 An example of basis function without capturing the effect of well located in the corner. 23

3.8 Figure (b) shows the basis function of the highlighted assemble dual coarse region of the 27×27 sample with one well in the corner which is now seen as pressure drop. Figure (a) is the well function of the corresponding well. 24

3.9 Well function containing fracture inside its domain of the well located at $[i, j] = [1, 1]$ for the sample shown in figure 3.3. 24

3.10 Results of test case 1: a) homogeneous permeability plot in logarithmic scale with well positioning. b) residual $(Ap - q)$ plot in logarithmic scale indicating non-zero values at dual coarse cell boundaries. c,d) pressure solution in 2D and 3D views. The graphs at left show the fine-scale pressure result (solved with 77×77 cells) where the graphs at right show multiscale pressure result (solved by 7×7 coarse cells) with significantly less number of DOFs. The coarsening ratio here is 11. The white lines indicate the boundaries of primal coarse grids. The plotted graph below the 3D multiscale graph in the right figure is the difference between fine-scale and multiscale solution. The normalized error is $\frac{\|p_{ms} - p_{fs}\|_2}{\|p_{fs}\|_2} = 8.24 \times 10^{-3}$ 28

3.11 Results of test case 2: a) heterogeneous permeability plot in logarithmic scale with fracture and well positioning. b) residual $(Ap - q)$ plot in logarithmic scale indicating non-zero values at dual coarse cell boundaries. c,d) pressure solution in 2D and 3D views. The graphs at left show the fine-scale pressure result (solved with 77×77 matrix cells and 36 fracture elements) where the graphs at right show multiscale pressure result (solved by 11×11 matrix coarse cells and 6 fracture course cells) with significantly less number of DOFs. The coarsening ratio here is 7. The white lines indicate the boundaries of primal coarse grids. The plotted graph below the 3D multiscale graph in the right figure is the difference between fine-scale and multiscale solution. The normalized error is $\frac{\|p_{ms} - p_{fs}\|_2}{\|p_{fs}\|_2} = 6.65 \times 10^{-3}$ 29

3.12 Results of test case 3: a) homogeneous permeability plot in logarithmic scale with fracture and well positioning. b) residual $(Ap - q)$ plot in logarithmic scale indicating non-zero values at dual coarse cell boundaries. c,d) pressure solution in 2D and 3D views. The graphs at left show the fine-scale pressure result (solved with 60×60 matrix cells and 92 fracture elements) where the graphs at right show multiscale pressure result (solved by 4×4 matrix coarse cells and 8 fracture course cells) with significantly less number of DOFs. The coarsening ratio here is 15. The white lines indicate the boundaries of primal coarse grids. The plotted graph below the 3D multiscale graph in the right figure is the difference between fine-scale and multiscale solution. The normalized error is $\frac{\|p_{ms} - p_{fs}\|_2}{\|p_{fs}\|_2} = 2.34 \times 10^{-2}$ 30

3.13 Results of test case 4: a) homogeneous permeability plot in logarithmic scale with fracture and well positioning. b) residual $(Ap - q)$ plot in logarithmic scale indicating non-zero values at dual coarse cell boundaries. c,d) pressure solution in 2D and 3D views. The graphs at left show the fine-scale pressure result (solved with 75×75 matrix cells and 92 fracture elements) where the graphs at right show multiscale pressure result (solved by 5×5 matrix coarse cells and 8 fracture course cells) with significantly less number of DOFs. The coarsening ratio here is 15. The white lines indicate the boundaries of primal coarse grids. The plotted graph below the 3D multiscale graph in the right figure is the difference between fine-scale and multiscale solution. The normalized error is $\frac{\|p_{ms} - p_{fs}\|_2}{\|p_{fs}\|_2} = 2.66 \times 10^{-2}$ 31

3.14	Results of test case 5: a) heterogeneous permeability plot in logarithmic scale with fracture and well positioning. b) residual $(Ap - q)$ plot in logarithmic scale indicating non-zero values at dual coarse cell boundaries. c,d) pressure solution in 2D and 3D views. The graphs at left show the fine-scale pressure result (solved with 91×91 matrix cells and 106 fracture elements) where the graphs at right show multiscale pressure result (solved by 7×7 matrix coarse cells and 10 fracture course cells) with significantly less number of DOFs. The coarsening ratio here is 13. The white lines indicate the boundaries of primal coarse grids. The plotted graph below the 3D multiscale graph in the right figure is the difference between fine-scale and multiscale solution. The normalized error is $\frac{\ p_{ms} - p_{fs}\ _2}{\ p_{fs}\ _2} = 5.58 \times 10^{-2}$	32
3.15	Results of test case 6: a) heterogeneous permeability plot in logarithmic scale with fracture and well positioning. b) residual $(Ap - q)$ plot in logarithmic scale indicating non-zero values at dual coarse cell boundaries. c,d) pressure solution in 2D and 3D views. The graphs at left show the fine-scale pressure result (solved with 99×99 matrix cells and 247 fracture elements) where the graphs at right show multiscale pressure result (solved by 9×9 matrix coarse cells and 27 fracture course cells) with significantly less number of DOFs. The coarsening ratio here is 11. The white lines indicate the boundaries of primal coarse grids. The plotted graph below the 3D multiscale graph in the right figure is the difference between fine-scale and multiscale solution. The normalized error is $\frac{\ p_{ms} - p_{fs}\ _2}{\ p_{fs}\ _2} = 7.22 \times 10^{-2}$	33
4.1	Construction of primal and dual coarse grids for a 1-level (left) and 2-level (right) MLMS method. The coarsening ratio here is 5 for both two multiscale levels.	36
4.2	Some of the basis functions of the sample used in fig. 4.1, 75×75 with coarsening ratio of 5. These basis functions belong to the coarse level 1.	38
4.3	The basis function in the central coarse node of the sample used in fig. 4.1, 75×75 with coarsening ratio of 5. This basis function belongs to the coarse level 2. Basis function is shown in 2D (left) and 3D (right) views.	39
4.4	F-MLMS strategy to obtain solution at coarsest level.	39
4.5	The two-point flux approximation (TPFA) fine system (left) considers connectivity of each fine-scale grid cell with only four direct neighbors whereas the multi-point flux approximation (MPFA) coarse system (right) accommodates the connectivity of each dual coarse with its diagonal neighbors as well. Computation of basis function for the first coarsening level uses TPFA fine system. For higher coarsening levels, MPFA coarse system is applied to obtain the basis functions.	40
4.6	Some matrix basis functions at coarsening level 1 (b,c) and the central matrix basis function at coarsening level 2 (d,e).	41
4.7	First and last basis functions of one of the fractures at coarsening level 1 (b,c) and coarsening level 2 (d,e).	42
5.1	Results of test case 1: a) homogeneous permeability plot in logarithmic scale with well positioning. b) residual $(Ap - q)$ plot in logarithmic scale indicating non-zero values at dual coarse cell boundaries. c,d) pressure solution in 2D and 3D views. The graphs at left show the finescale pressure result (solved with 81×81 cells) where the graphs at right show MLMS pressure result (solved by 3×3 coarse cells) with significantly less number of DOFs. The coarsening level is 3 and the coarsening ratio is 3. The white lines indicate the boundaries of primal coarse grids. The plotted graph below the 3D MLMS graph in the right figure is the difference between finescale and MLMS solution. The normalized error is $\frac{\ p_{ms} - p_{fs}\ _2}{\ p_{fs}\ _2} = 2.71 \times 10^{-2}$	46

5.2	Results of test case 2: a) heterogeneous permeability plot in logarithmic scale with well positioning. b) residual $(Ap - q)$ plot in logarithmic scale indicating non-zero values at dual coarse cell boundaries. c,d) pressure solution in 2D and 3D views. The graphs at left show the finescale pressure result (solved with 100×100 cells) where the graphs at right show MLMS pressure result (solved by 4×4 coarse cells) with significantly less number of DOFs. The coarsening level is 2 and the coarsening ratio is 5. The white lines indicate the boundaries of primal coarse grids. The plotted graph below the 3D MLMS graph in the right figure is the difference between finescale and MLMS solution. The normalized error is $\frac{\ p_{ms} - p_{fs}\ _2}{\ p_{fs}\ _2} = 3.27 \times 10^{-2}$	47
5.3	Results of test case 3: a) homogeneous permeability plot in logarithmic scale with fracture and well positioning. b) residual $(Ap - q)$ plot in logarithmic scale indicating non-zero values at dual coarse cell boundaries. c,d) pressure solution in 2D and 3D views. The graphs at left show the finescale pressure result (solved with 135×135 matrix cells and 82 fracture elements) where the graphs at right show MLMS pressure result (solved by 5×5 matrix coarse cells and 4 fracture course cells) with significantly less number of DOFs. The coarsening level is 3 and the coarsening ratio is 3. The white/grey lines indicate the boundaries of primal coarse grids. The plotted graph below the 3D MLMS graph in the right figure is the difference between finescale and MLMS solution. The normalized error is $\frac{\ p_{ms} - p_{fs}\ _2}{\ p_{fs}\ _2} = 1.16 \times 10^{-2}$	48
5.4	Results of test case 4: a) heterogeneous permeability plot in logarithmic scale with fractures and well positioning. b) residual $(Ap - q)$ plot in logarithmic scale indicating non-zero values at dual coarse cell boundaries. c,d) pressure solution in 2D and 3D views. The graphs at left show the finescale pressure result (solved with 100×100 matrix cells and 152 fracture elements) where the graphs at right show F-MLMS pressure result (solved by 4×4 matrix coarse cells and 8 fracture course cells) with significantly less number of DOFs. The coarsening level is 2 and the coarsening ratio is 5. The white/grey lines indicate the boundaries of primal coarse grids. The plotted graph below the 3D MLMS graph in the right figure is the difference between finescale and MLMS solution. The normalized error is $\frac{\ p_{ms} - p_{fs}\ _2}{\ p_{fs}\ _2} = 4.40 \times 10^{-2}$	49
5.5	Results of test case 5: a) homogeneous permeability plot in logarithmic scale with fractures and well positioning. b) residual $(Ap - q)$ plot in logarithmic scale indicating non-zero values at dual coarse cell boundaries. c,d) pressure solution in 2D and 3D views. The graphs at left show the finescale pressure result (solved with 75×75 matrix cells and 380 fracture elements) where the graphs at right show F-MLMS pressure result (solved by 3×3 matrix coarse cells and 20 fracture course cells) with significantly less number of DOFs. The coarsening level is 2 and the coarsening ratio is 5. The white/grey lines indicate the boundaries of primal coarse grids. The plotted graph below the 3D MLMS graph in the right figure is the difference between finescale and MLMS solution. The normalized error is $\frac{\ p_{ms} - p_{fs}\ _2}{\ p_{fs}\ _2} = 7.85 \times 10^{-2}$	50
5.6	Test case 6: homogeneous permeability plot in logarithmic scale with fractures and well positioning. The sample has 81×81 matrix cells and 164 fracture elements.	51
5.7	Test case 6: Pressure solution with different coarsening levels ratios. The second norm error is calculated by equation (3.5.1).	52

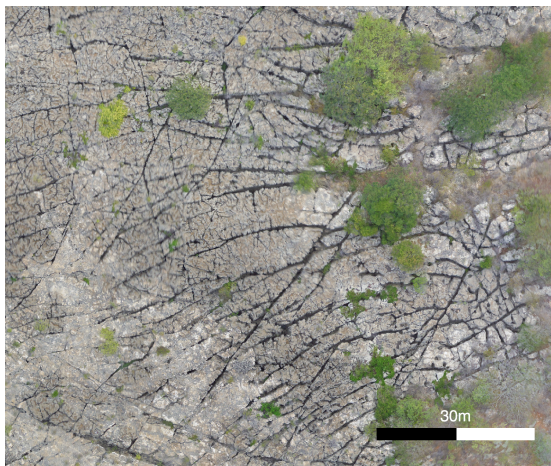
Chapter 1

Introduction

Many of the water and hydrocarbon reservoirs around the world are naturally fractured (See Fig. 1.1 as real-field outcrop examples). Depending on the tectonic forces and the lithology, the length scales, the size and the distribution of the fractures in natural formation can be extremely diverse. Some reservoirs present a few disconnected fractures while others have very complex fracture networks [3].

Fractures usually have very small apertures (i.e., at the scale of millimeters). Even though their volume is relatively small and they do not contain considerable amount of fluids, they are typically highly conductive (several orders of magnitude more than the rock). Therefore, they play an important role in transporting fluids through the formation.

The significant effect of fractures on fluid flow and transport makes it vital for reservoir simulation and management studies to consider an accurate modeling of fractures in many real scenarios (such as underground water resources, hydrocarbon and geothermal reservoirs, etc.). However, the geometrical complexity of the fractured media together with the large conductivity contrasts between fracture and matrix impose a huge challenge to simulators. High computational costs together with low accuracy of the excessively upscaled models have made such simulations incapable of providing satisfactory results for field-scale problems. Consequently, many specialists are working to improve the efficiency of simulations by introducing new techniques and approaches in modeling flow in fractured media.



(a) Potiguar Basin, Apodi, Rio Grande Do Norte, Brazil



(b) Brochterbeck quarry, Germany

Figure 1.1: a) Fracture network in flat-lying carbonates in the Potiguar Basin, Apodi, Rio Grande Do Norte, Brazil. Photo made by K. Bisdom, PhD Candidate, TU Delft [2]. b) Fractures together with inclined layering, Brochterbeck quarry, Germany. Photo taken by the author.

1.1. Fracture Modeling Approaches

Different approaches have been proposed to model the effect of fractures on the displacements of fluids in natural formations. One option, known as fully-resolved approach or DNS (Direct Numerical Simulation), is to explicitly account for fractures by adapting the grid to their geometry and resolution. However, due to their tiny aperture, this requires to employ extremely high resolution grids, not compatible with the length scales of natural formations. As a consequence, this approach is not practical for field scale studies.

Alternately, it is possible to upscale fractures by averaging their permeability with matrix permeability introducing a porous media representation without fractures but with approximated conductivity. However, such model rises concerns about inaccuracy of the simulation results due to the employed excessively upscaled parameters, specially in presence of high conductivity contrasts between the matrix and fractures.

Therefore, scientists and specialists introduced two distinct methods in the fracture modeling approach; the so called dual permeability model (also known as dual continuum or dual porosity) [4, 5, 6] and the discrete fracture model (DFM) [7].

In the former method, the matrix plays the role of fluid storage and the fluid only flows inside the fractures. As it is assumed that there is no direct connection between the matrix cells, this model neglects the flow through the porous rock.

DFM considers fractures as a separate system in a lower dimensional space than that of the matrix, and couples them through a transfer function. DFM provides more accurate results. Thus, it has been developed and evolved quite significantly during the past several years (See, e.g., [2, 8, 9, 10, 11, 12, 13, 14, 15], and the references therein). Next, the DFM approaches are being explained in brief.

1.2. Discrete Fracture Models (DFM)

Two different DFM approaches have been presented in the literature: the Embedded DFM (EDFM) and the Conforming DFM (CDFM). The main difference between these two techniques resides in the flexibility to the grid geometry. An illustration of these methods is presented in Fig. 1.2.

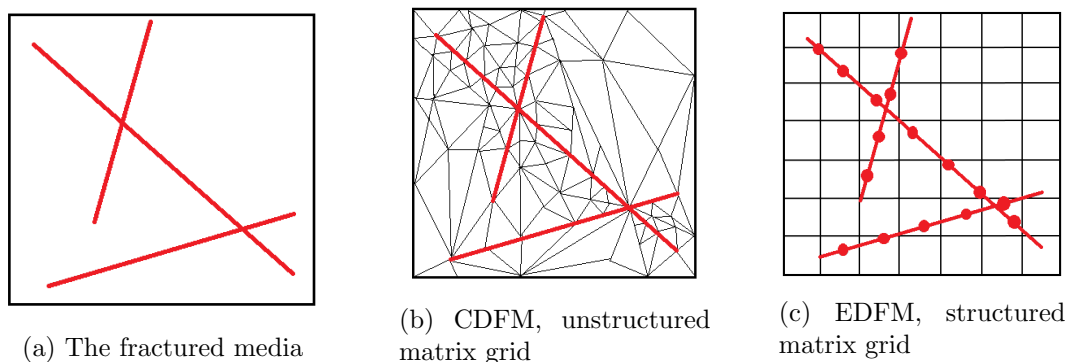


Figure 1.2: A schematic sample showing the grid construction of different DFM approaches.

1.2.1. Conforming Discrete Fracture Model (CDFM)

In CDFM, fracture elements are located at the interfaces between the triangular unstructured matrix grid-cells. The effect of fractures is represented by modifying transmissibilities at those interfaces. Therefore, there is an accurate consideration of flux transfer between matrix and fracture. However for highly dense fracture networks the number of matrix grid cells should be very

high with very fine triangles close to the fracture intersections, to account for the fractures. In addition, in case of fracture generation and propagation, the matrix grid has to be redefined at each time-step which reduces the efficiency of such approach. All of these complexities can limit the application of CDFM in real-field applications [16].

1.2.2. Embedded Discrete Fracture Model (EDFM)

In EDFM, fractures are discretized separately from the matrix and then coupled with it using a flux transfer term [8, 17]. Having two independent grids allows for modeling of complex fracture networks even with simple grids for the matrix. However, one limitation of EDFM is its applicability to fractures with low conductivity compared to the matrix. In order to deal with this limitation, projected EDFM (pEDFM) has been recently introduced [18].

1.3. Multiscale Methods

Hydrocarbon reservoirs have large length scales (orders of kilometers) and are highly heterogeneous sometimes with high contrast in relatively small distances. Accurate numerical simulations require high resolution grids in order to honor the heterogeneity of the geological properties of natural formations. However, such grid refinement results in multi-billion cell problems which cannot be efficiently solved with the state-of-the-art computational capacity [19]. One option is to upscale the fine-scale properties and reduce the degrees of freedom dealing with a smaller amount of unknowns. However, such approach may lead to inaccurate solution for highly heterogeneous formations. In addition to this, a prior estimate of the error cannot be obtained [20, 21]. The multiscale finite volume method (MSFV) was developed to provide an approximate solution of the fine-scale system [22, 19].

Several multiscale methods exist (See e.g. [23, 24, 25, 26, 27, 28, 29, 30, 31] and references therein). In fluid mechanics, Multiscale Finite Volume Method (MSFV) is used as it fulfills the mass conservation law for fluid flow. However, MSFV does not always provide solution with practical accuracy. In case of high heterogeneity or anisotropy contrasts, the accuracy of MSFV is greatly and negatively affected. In order to defeat this deficiency, iterative MSFV (i-MSFV) method has been introduced with the help of efficient algorithm that converges to the fine-scale solution [32].

Combining EDFM with MSFV, the multiscale approach helps increasing the efficiency of fluid flow simulation in fractured reservoirs. Note that most of the MSFV developments so far have been focused on two grid resolutions (fine and one-level coarse) only. Of particular interest of the computational geoscience community, and the focus of this work, is to develop a multilevel coarse grid resolutions of the explicit EDFM fracture modeling approach.

1.4. Multilevel Multiscale Approach (MLMS)

Multiscale approach is considered as a great help with enough accuracy to decrease the computational cost. It is feasible to benefit from MSFV application to solve problems within the range of a million grid cells. However, much larger problems with millions to billions of grid cells often occur in field applications for which we need a more advanced method to provide a more efficient and faster solution. In order to overcome such issue, it is applicable to extend the concept of MSFV from only one level into multiple levels of multiscale to increase the efficiency even further [33]. The Multi Level Multi Scale finite volume method (MLMS) approach uses the same method as in MSFV recursively by giving the primal coarse cells of 1st coarsening level to next level of coarsening and so on (See chapter 4 for more details). For porous media containing high heterogeneity contrasts, MLMS suffers the same inaccuracy as in MSFV approach. Therefore, iterative multiscale here also can be used to achieve convergence to the fine-scale solution.

1.5. Multilevel Multiscale Method for Fractured porous media (F-MLMS)

Now that EDFM and MLMS are briefly described, one should notice the advantage of their combination to reach an advanced numerical approach in order to achieve a greater efficiency with capability of implementing multiple levels of coarsening for embedded discrete fracture modeling. Primal and dual coarse grid structure is generated both for the matrix and the fracture network at each coarse level recursively. Thereafter, the approximate solution is provided at the fine-scale resolution both in the matrix and in the fractures.

1.6. Research Goals

EDFM and MSFV approaches and its implementations have been fully described in the above-mentioned literature. However, MLMS is a recently introduced concept which requires and accurate algorithmic development, validation, and systematic performance and sensitivity studies which are all missing in the literature. In addition, the multilevel multiscale approach for fractured porous media (F-MLMS) is introduced and studied for the first time in this thesis.

The main goals of this MSc thesis report is to develop an accurate MLMS approach and to devise the first multilevel multiscale approach for fractured porous media (F-MLMS). Therefore in this thesis, the research goals can be summarized as following:

- Development of an accurate multilevel multiscale method (MLMS)
- Devise a Multilevel Multiscale finite volume method for Fractured porous media (F-MLMS).

The thesis is structured as following. In chapter 2, EDFM is briefly described and results of some test cases are analyzed. Chapter 3 includes implementation of multiscale finite volume method for EDFM. Thereafter, in chapter 4, multilevel multiscale approach is explained and its implementation for EDFM as multilevel multiscale method for fractured porous media (F-MLMS) is introduced and devised as the main focus of this work. Finally, in chapter 5, the results and discussions for MLMS and F-MLMS are covered. Conclusion is available in chapter 6.

Note that all developments presented in the following chapters are based on the developed MATLAB simulator, which is developed by the author from scratch. As such, a significant code development throughout the course of this thesis work, along with the method and algorithmic developments, was performed.

Chapter 2

Embedded Discrete Fracture Model (EDFM)

After revisiting a few basic parameters describing fractures, the Embedded Discrete Fracture Model [8, 17] is briefly described in this chapter. At the end, results for some selective test cases are presented.

2.1. Description of Fracture Network

Rocks in natural formations are porous media presenting a complex network of fractures, crossing each other and penetrating at any possible location. Each fracture has its own properties such as length, aperture and permeability, some of which (e.g. aperture and permeability) can even vary through the length of an individual fracture. Fracture network is defined as the set of entire connected fracture lines, in which each fracture can be of any length scale. The aperture of each fracture is the effective gap between the fracture plates (lines in 2D domains). In this work, we assign these parameters to the fracture system as input of our model. Fractures are often highly conductive compared to the matrix. It is possible to calculate the permeability of a fracture as flow between parallel plates, which leads to

$$k = b^2/12, \tag{2.1.1}$$

where k [m^2] is the permeability of the fracture and b [m] is its aperture (can change through the fracture length). As an example, a fracture with $b = 1$ [mm] aperture has a permeability of approximately 83.3 Darcy.

2.2. EDFM Formulation

Based on EDFM method, the fractured porous media is split into a separate matrix grids and fracture elements independent from each other in terms of grid structuring. In this report the porous media is considered as 2D medium and therefore fractures are 1D channels discretized independently from the matrix grid (see Fig. 2.1).

Once the computational grids are imposed, mass balance equations for matrix and fractures, i.e.,

$$\frac{\partial}{\partial t} (\phi S_\alpha)^m - \nabla \cdot (\lambda_\alpha \cdot \nabla p)^m = q_\alpha^m + \Psi_\alpha^{mf} \tag{2.2.1}$$

and

$$\frac{\partial}{\partial t} (\phi S_\alpha)^f - \nabla \cdot (\lambda_\alpha \cdot \nabla p)^m = q_\alpha^f + \Psi_\alpha^{fm}, \tag{2.2.2}$$

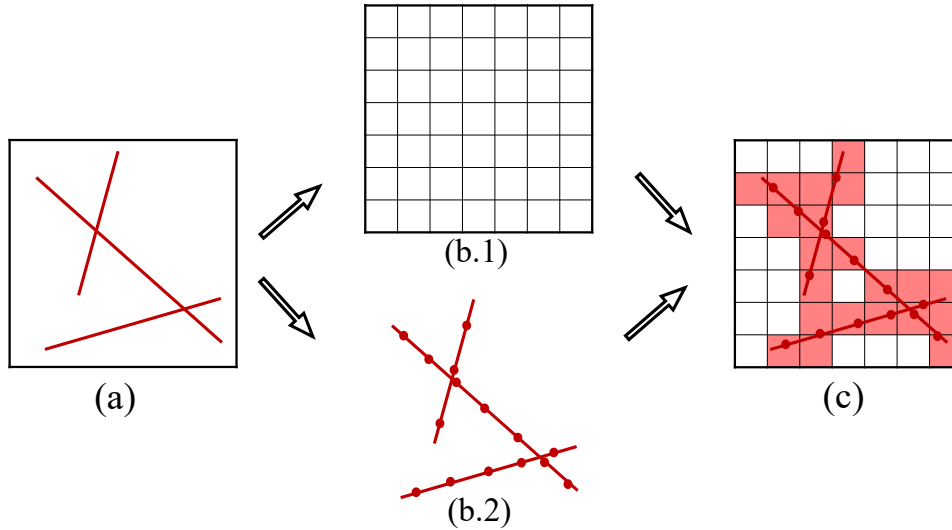


Figure 2.1: Schematic of EDFM concept. The fractured media (a) is independently split into a matrix grid system (b.1) and a fracture network grid (b.2). Also the matrix and fracture grids are showed on top of each other (c) with overlapped matrix cells highlighted with color.

are solved, respectively. Here, ϕ is the porosity, S_α is the saturation of phase α . Moreover, p is the pressure, λ_α is the phase mobility which can be written as $\lambda_\alpha = k k_{r\alpha} / \mu_\alpha$. Note that $k_{r\alpha}$ and μ_α are the relative permeability and the viscosity of phase α , respectively, and k is the absolute rock permeability.

Following IMPES (Implicit Pressure Explicit Saturation) simulation strategy, one first obtains pressure equations and then couple them to transport equation of one of the 2 phases. The pressure equation for EDFM system finally reads

$$-\nabla \cdot (\lambda_t \cdot \nabla p)^m = q_t^m + \Psi^{mf} \quad (2.2.3)$$

and

$$-\nabla \cdot (\lambda_t \cdot \nabla p)^f = q_t^f + \Psi^{fm} \quad (2.2.4)$$

for matrix and fractures, respectively.

In EDFM, the fracture-matrix connectivities are defined through Ψ^{mf} and Ψ^{fm} parameters, which read

$$\Psi_V^{mf} = CI \lambda_t (p^f - p^m) / V \quad (2.2.5)$$

and

$$\Psi_A^{fm} = CI \lambda_t (p^m - p^f) / A \quad (2.2.6)$$

respectively. Here, CI is the co-called "Connectivity Index" between matrix and fracture and is a grid-dependent property [17] (see section 2.3).

Note that fractures are considered to have a lower dimensional mathematic domain, resulting in division-by-volume term in matrix-fracture flux and division-by-area term in fracture-matrix flux [17]. The local mass balance would ensure the amount of total fluid which leaves the matrix is exactly the same as the amount entering the fractures (and vice versa), i.e.,

$$\int_V \Psi_V^{mf} dV = \int_A \Psi_A^{fm} dA. \quad (2.2.7)$$

2.3. Discretized Form of the Pressure Equation

In order to clearly describe the discrete pressure equation, let us consider the following 2D example as shown in Fig. 2.2.

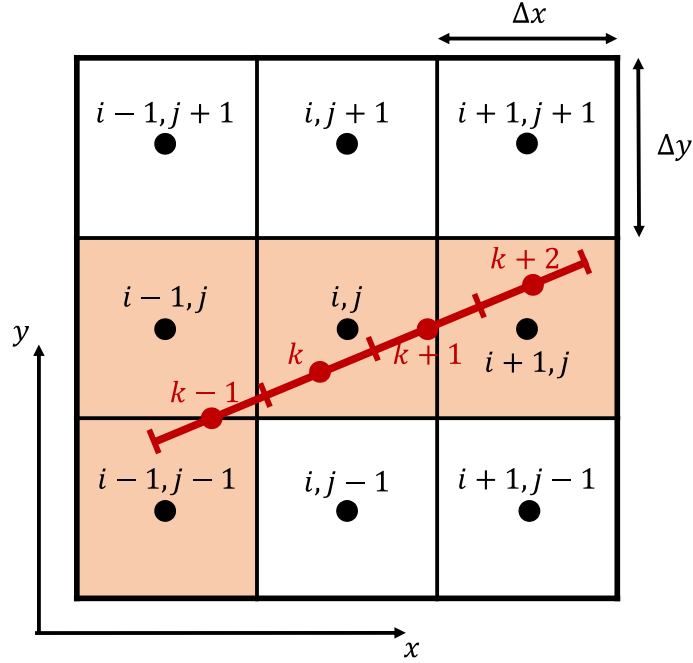


Figure 2.2: Matrix cell (i, j) with its surrounding cells and fracture elements overlapping the matrix cells in this region. Here, fracture elements $k-1$, k and $k+1$ have penetrated the matrix cell (i, j) .

The discretization of the pressure equation for matrix cell (i, j) in Fig. 2.2 is expressed as the following:

$$\begin{aligned} \frac{\Delta A_x \lambda_{t,x}^{i-1/2,j}}{\Delta x} (p_{i,j} - p_{i-1,j}) + \frac{\Delta A_x \lambda_{t,x}^{i+1/2,j}}{\Delta x} (p_{i,j} - p_{i+1,j}) + \\ \frac{\Delta A_y \lambda_{t,y}^{i,j-1/2}}{\Delta y} (p_{i,j} - p_{i,j-1}) + \frac{\Delta A_y \lambda_{t,y}^{i,j+1/2}}{\Delta y} (p_{i,j} - p_{i,j+1}) = \\ \sum_{\Omega_{i,j} \cap \Omega_k} C I_k \lambda_{t,i,j,k} (p_k - p_{i,j}), \end{aligned} \quad (2.3.1)$$

where ΔA_x and ΔA_y are cross sectional areas in x and y directions, respectively. $\Omega_{i,j}$ and Ω_k are control domains of matrix cell (i, j) and fracture element k , respectively. Also, $\lambda_{t,i,j,k}$ is harmonically averaged mobility between matrix cell (i, j) and the corresponding fracture element k . Note that the \sum sign adds up the flux transfers between the matrix cell (i, j) and each of the overlapping fracture elements (here, $k-1$, k and $k+1$).

Similar to equation (2.3.1), the discretization of the pressure equation for fracture element k is written as

$$\frac{\Delta A_f \lambda_t^{k-1/2}}{\Delta L_f} (p_k - p_{k-1}) + \frac{\Delta A_f \lambda_t^{k+1/2}}{\Delta L_f} (p_k - p_{k+1}) = \sum_{\Omega_k \cap \Omega_{i,j}} C I_{i,j} \lambda_{t,i,j,k} (p_{i,j} - p_k) \quad (2.3.2)$$

In this equation, ΔL_f and ΔA_f are the length and cross sectional area of fracture element k .

2.3.1. Connectivity Index

The connectivity index CI between matrix cell (i, j) and fracture element k is defined as area fraction of that fracture element inside the overlapped matrix cell ($A_{ij,k}$) divided by the average distance between the matrix cell and the fracture element ($\langle d \rangle_{ij,k}$) [17]:

$$CI_{ij,k} = \frac{A_{ij,k}}{\langle d \rangle_{ij,k}} \quad \text{with} \quad \langle d \rangle_{ij,k} = \frac{\int x_n(\mathbf{x}') d\mathbf{x}'}{V_{ij}}. \quad (2.3.3)$$

The area fraction of the corresponding fracture element k in matrix cell (i, j) is simply the lateral area of both plates of fracture that are located inside the matrix cell depending on whether the fracture cuts through the matrix cell or just touches the boundaries of it (only one plate of fracture having overlap with the matrix cell).

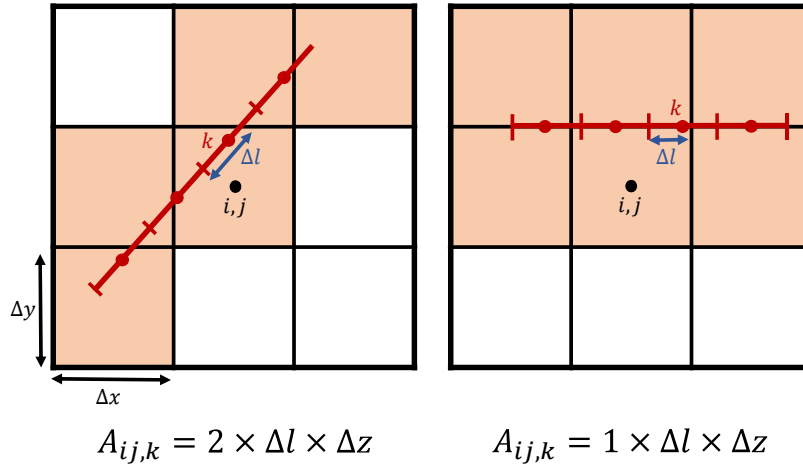


Figure 2.3: The area fraction calculation for connectivity index for 2 different cases.

In order to calculate the average distance between the fracture element and the matrix cell, as it is mentioned in equation (2.3.3), it is possible to use analytical method which provides the advantage over numerical methods in terms of efficiency [17] [16]. Figure 2.4 shows the calculation of $\langle d \rangle_{ij,k}$ for different cases based on the position of fracture element inside the matrix cell.

2.3.2. Fracture Intersection

For the fracture part of the domain, the transmissibilities between the elements of one fracture is rather simple. However, in case of intersection between two or more fractures, it is needed to use a more generalized method to obtain the transmissibilities, a method which is similarly used in electrical circuits called star-delta transformation. Assume two fractures f_1 and f_2 have intersection. Generally, there are four fracture elements (two from each fracture) connected to each other through this intersection. The transmissibility between each two elements (k and l) is written as [2] [16]:

$$T^{l,m} \simeq \frac{\alpha_l \alpha_m}{\sum_{k=1}^n \alpha_k}, \quad \text{where} \quad \alpha_k = \frac{A_f^k \lambda_t^k}{\frac{1}{2} L^k}. \quad (2.3.4)$$

To better understand this method, assuming the fracture intersection in the figure 2.5, the transmissibility between fracture elements 1 and 2 is obtained as [16]:

$$T^{1,2} \simeq \frac{\alpha_1 \alpha_2}{\alpha_1 + \alpha_2 + \alpha_3 + \alpha_4}. \quad (2.3.5)$$

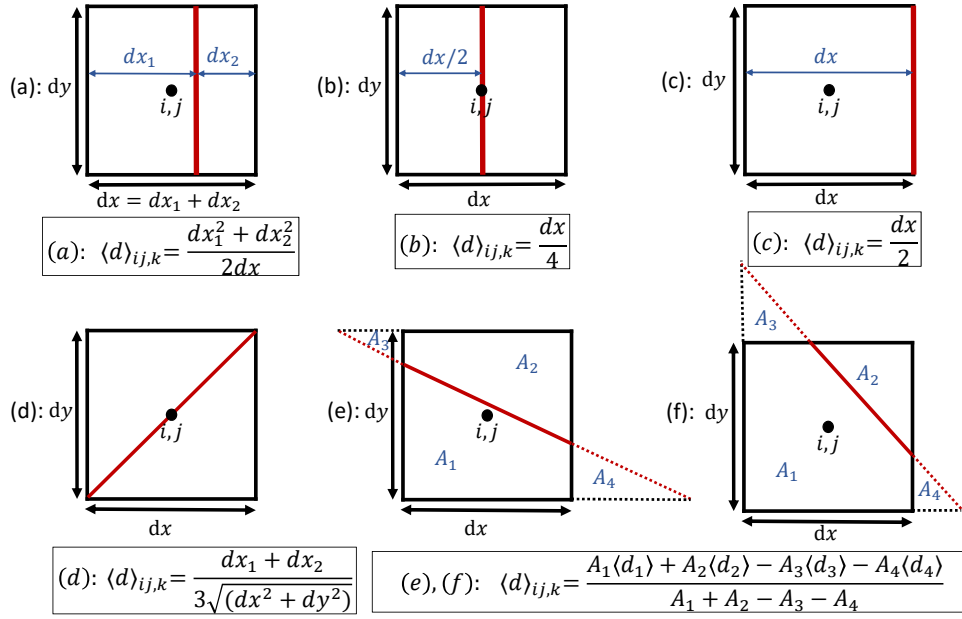


Figure 2.4: Calculation of average distance between fracture element and matrix cell ($\langle d \rangle_{ij,k}$) for different cases.

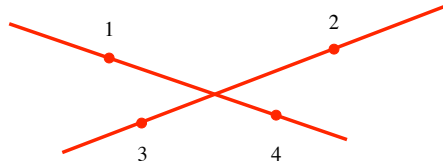


Figure 2.5: Intersection between two fractures. The nodes in the figure are the centers of each fracture elements.

2.3.3. The system of pressure equations

Now, by knowing all the parameters, we can put the equations in a linear system and solve the pressure. The linear system is gathered as $\mathbf{A}\mathbf{p} = \mathbf{q}$ which couples the pressure equations of matrix and fracture. In order to have a better structured matrix system, the transmissibilities between each matrix cell, fracture element and well are put into the coefficient matrix \mathbf{A} , the pressures are stacked in to the vector \mathbf{p} and the source terms in \mathbf{q} .

$$\begin{bmatrix} \mathbf{A}_{mm} & \mathbf{A}_{mf} & \mathbf{A}_{mw} \\ \mathbf{A}_{fm} & \mathbf{A}_{ff} & \mathbf{A}_{fw} \\ \mathbf{A}_{wm} & \mathbf{A}_{wf} & \mathbf{A}_{ww} \end{bmatrix} \begin{bmatrix} \mathbf{p}_m \\ \mathbf{p}_f \\ \mathbf{p}_w \end{bmatrix} = \begin{bmatrix} \mathbf{q}_m \\ \mathbf{q}_f \\ \mathbf{q}_w \end{bmatrix}, \quad (2.3.6)$$

Here, \mathbf{A} is the matrix of coefficient relating the pressure of elements to each other which consists of nine blocks. \mathbf{A}_{mm} , \mathbf{A}_{ff} and \mathbf{A}_{ww} contain matrix-matrix, fracture-fracture and well-well transmissibilities respectively. \mathbf{A}_{mf} and \mathbf{A}_{fm} , contain the transmissibilities between the matrix and fractures (and vice versa). \mathbf{A}_{mw} and \mathbf{A}_{wm} similarly include the matrix-well and well-matrix transmissibilities. The same holds for \mathbf{A}_{fw} and \mathbf{A}_{wf} as fracture-well and well-fracture transmissibilities. \mathbf{q}_m , \mathbf{q}_f and \mathbf{q}_w are matrix, fracture and well source terms stacked together to form the source term vector \mathbf{q} . \mathbf{p}_m , \mathbf{p}_f and \mathbf{p}_w are stacked together to form the pressure vector. The advantage of including the well pressures into the system of equation and treating them as unknowns, is that in

Table 2.1: The identical parameters for all test cases

$L_x = 100.0 [m]$, $L_y = 100.0 [m]$	Length of the reservoir in the x and y direction
$k_{rw_e} = 0.7$, $k_{ro_e} = 0.6$	End-point relative permeabilities
$s_{wc} = 0.2$, $s_{or} = 0.1$	Connate water and residual oil saturations
$n_w = 3.0$, $n_o = 2.0$	Saturation exponents
$\mu_w = 0.001 [pa.s]$, $\mu_o = 0.01 [pa.s]$	Fluid viscosities
$\phi = 0.3$	Porosity
$WI = 1000$	Well Index
$P_{injection} = 3.0$, $P_{production} = 0.0$	Pressure inside injection and production wells
$k_f/k_m = 10^5$	Permeability contrast between fracture and matrix
$W_f = 5 [mm]$	Fracture aperture

case of having wells with flow-rate constraint condition, the pressures at such wells are then simply obtained by solving the linear system. In case of pressure constraint wells, those equations are simply reduced into Dirichlet boundary conditions. Pressure is achieved by: $\mathbf{p} = \mathbf{A}^{-1} \mathbf{q}$

For phase transport equations, first, the velocities are calculated from the pressure solution through Darcy's law, i.e., $u_t = -\lambda_t \nabla p$. Then an explicit method is used to solve phase saturation, with time-step sizes which satisfy the CFL condition [34]. This forms an IMPES (Implicit Pressure Explicit Saturation) simulation strategy, an overview of which is presented in Fig. 2.6. Note that for all multiphase solutions of this work, the Brooks-Corey relative permeability function is used.

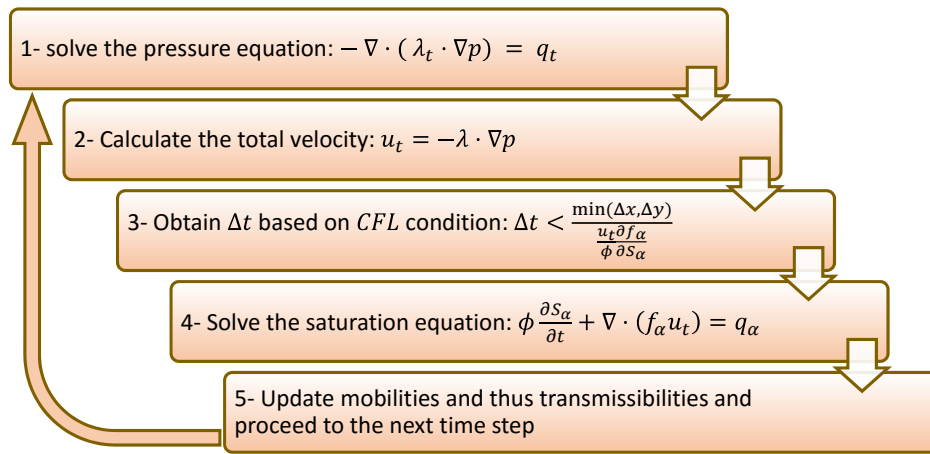


Figure 2.6: IMPES method flowchart.

2.4. EDFM Results and Verification of the Developed Simulator

In this work, EDFM method implementation is done for 2D domain in MATLAB simulator. Some test cases are studied and tested by the simulator either for only the pressure solution or both pressure and saturation results. In all test cases, ΔL_f is similar to the size of Δx and Δy . Some parameters are identical for all test cases, which are described in table 2.1. In the caption of the results, explanations of each test case is provided. Also, a discussion paragraph concludes the revisit and development of EDFM simulator of this project.

2.4.1. Test Case 1: Quarter of Five Spot with One Diagonal Fracture

In this test case, there is one injection well at bottom left and one production well at top right of the domain. One fracture lies diagonally (SW-NE) in the center. The media consists of $50 \times 50 = 2500$ matrix cells and 39 fracture elements. Results are shown in figure 2.7.

2.4.2. Test Case 2: Line drive with Two Fracture Perpendicular to each other, "+" Shape

In this test case, 5 injection wells are located at left boundary and 5 production wells are located at right boundary of the domain. Two fractures form "+" sign in the center. The media consists of $50 \times 50 = 2500$ matrix cells and $2 \times 40 = 80$ fracture elements (See Fig. 2.8).

2.4.3. Test Case 3: Line drive with Two Fracture Perpendicular to each other, "x" Shape

In this test case, similar to test case 2, 5 injection wells are located at left boundary and 5 production wells are located at right boundary of the domain. Two fractures form "x" sign in the center. The media consists of $50 \times 50 = 2500$ matrix cells and $2 \times 40 = 80$ fracture elements. Figure 2.9 shows the result for this test case.

2.4.4. Test Case 4: Series of Intersected Fractures

Now, as a mean to observe the effect of flow crossover between fractures, let us assume a test case with 5 fractures having intersection with each other (one on one) as shown in figure 2.10. Here, the matrix consists of $50 \times 50 = 2500$ cells with total number of 142 fracture elements. There are 5 injection wells (left boundary) and 5 production wells (right boundary). One fracture has overlap with bottom left matrix cell containing an injection well.

2.5. Discussion

Presence of fracture in all test cases has significant effect on fluid flow. As it can be observed, the pressure gradient inside the fracture is much smaller than that of matrix both at initial state and final state. The more directed the fracture alignment towards the flow path, the higher the amount of transported flow by the fracture. One can conclude that breakthrough is greatly impacted by presence of fractures especially those with alignment parallel to the matrix main pressure gradient.

Although EDFM provides a more efficient solution compared to a fully resolved (DNS) approach, yet a multiscale approach is needed to improve the efficiency for real-field applications. This will be explained briefly in the next chapter.

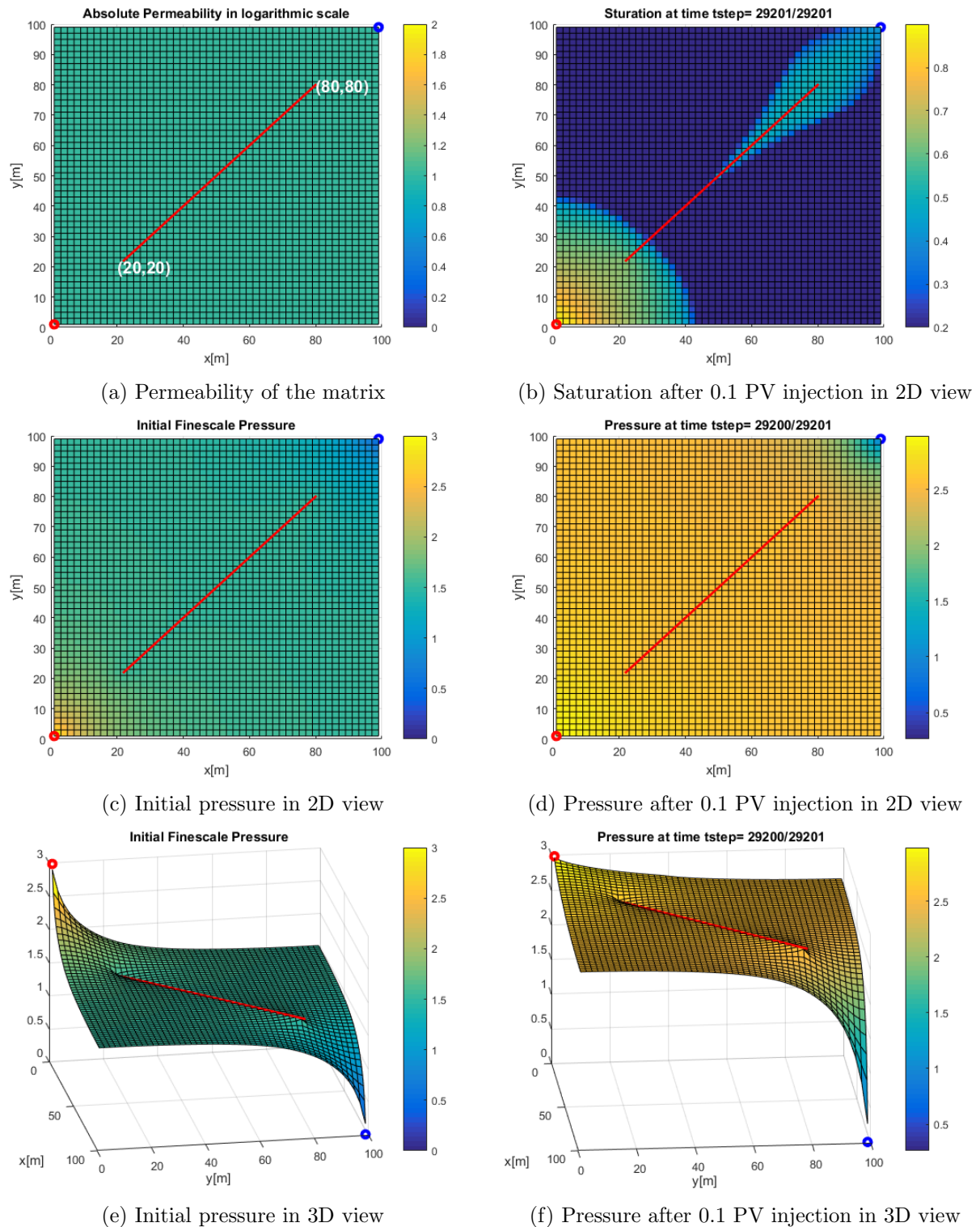


Figure 2.7: Results of test case 1: a diagonal fracture having significant effect on the productivity of the reservoir.

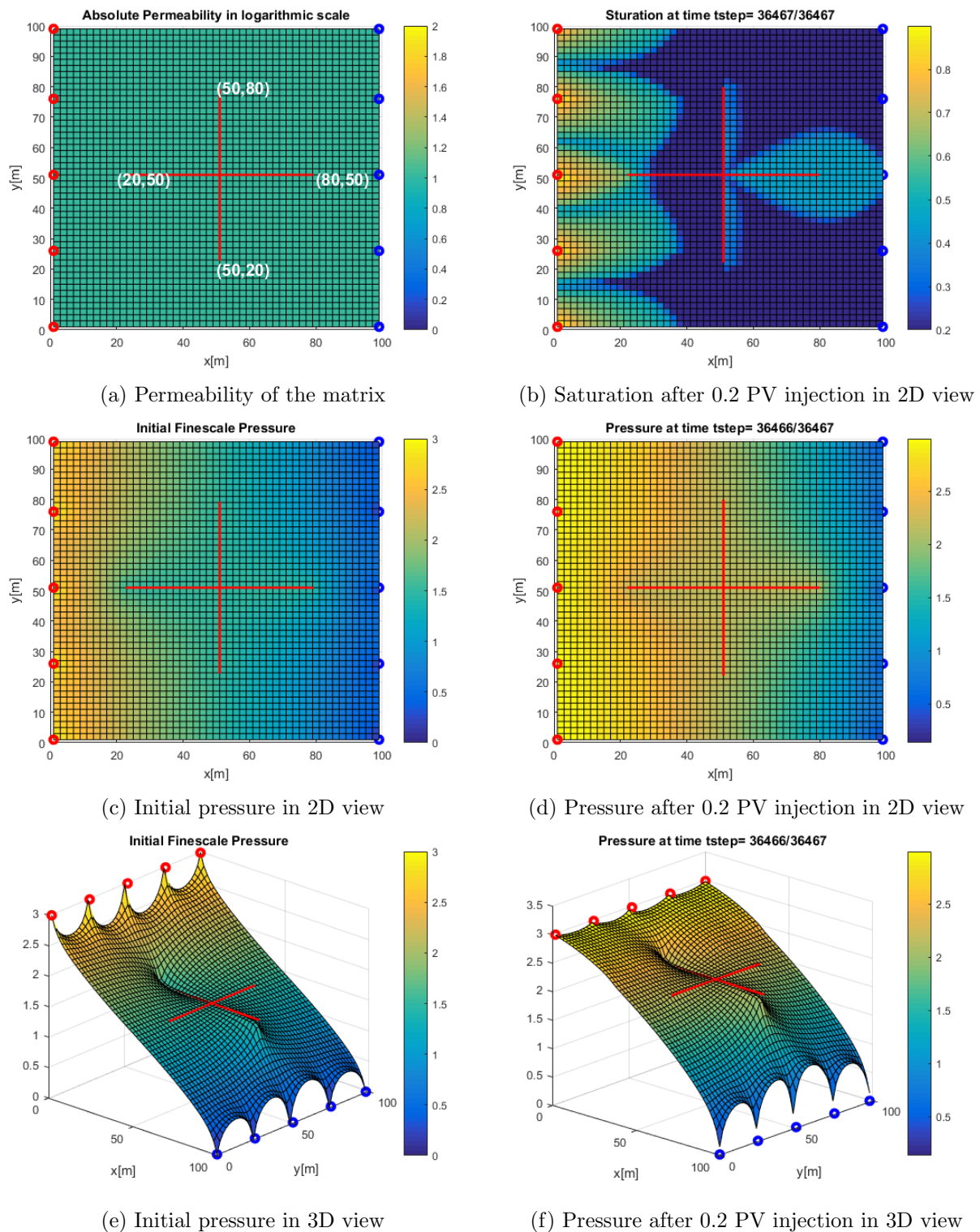
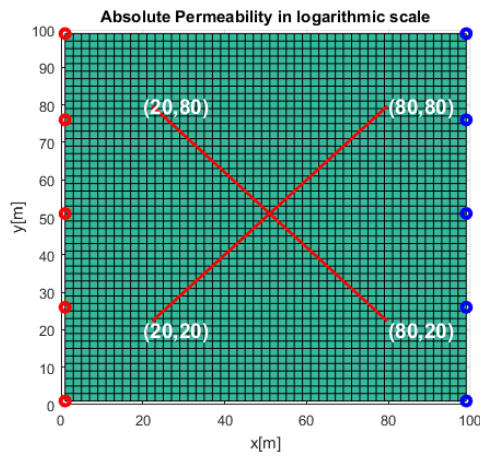
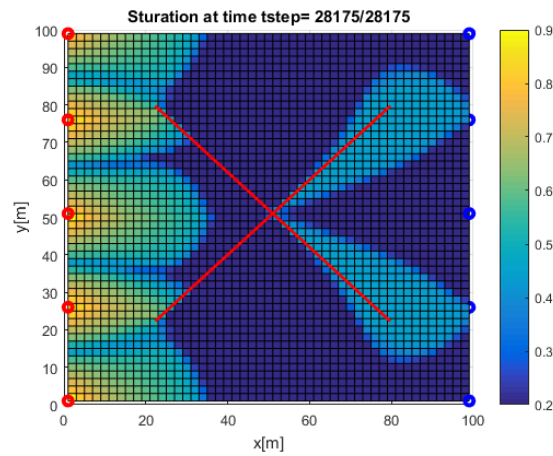


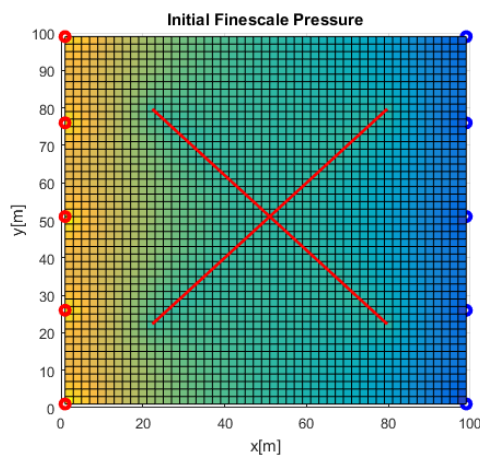
Figure 2.8: Results of test case 2: a cross-shaped fracture being accurately captured through EDFM formulation. Note that due to high conductivity of the fracture network the pressure drop inside fractures is very small, compared with that of the matrix rock.



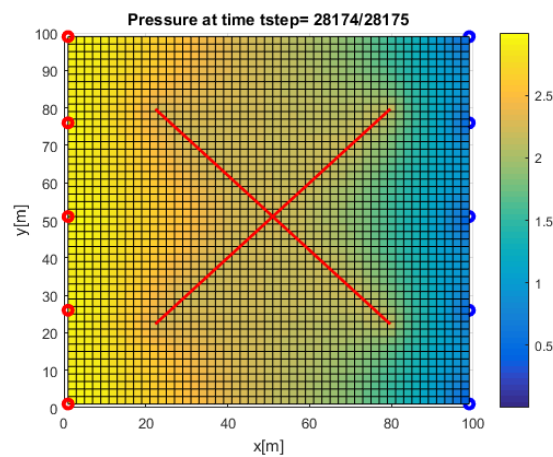
(a) Permeability of the matrix



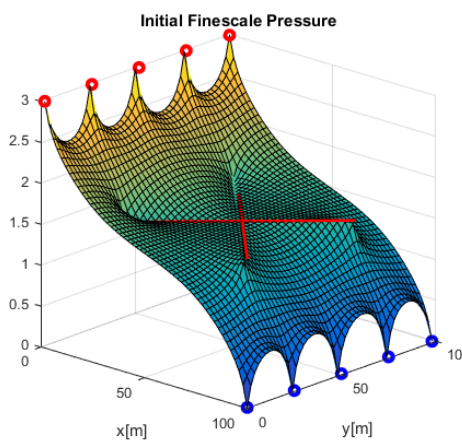
(b) Saturation after 0.2 PV injection in 2D view



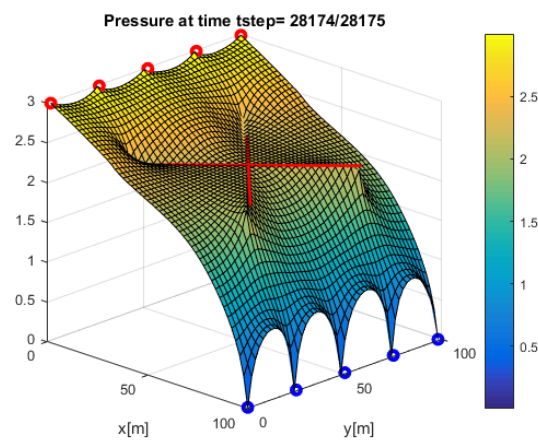
(c) Initial pressure in 2D view



(d) Pressure after 0.2 PV injection in 2D view



(e) Initial pressure in 3D view



(f) Pressure after 0.2 PV injection in 3D view

Figure 2.9: Results of test case 3: diagonal-shape fracture network being independently discretized along with the matrix grid cell. This test case illustrates the advantage of EDFM over DFM in terms of grid complexity, as no adjustment of matrix grid cells for fractures is necessary in EDFM.

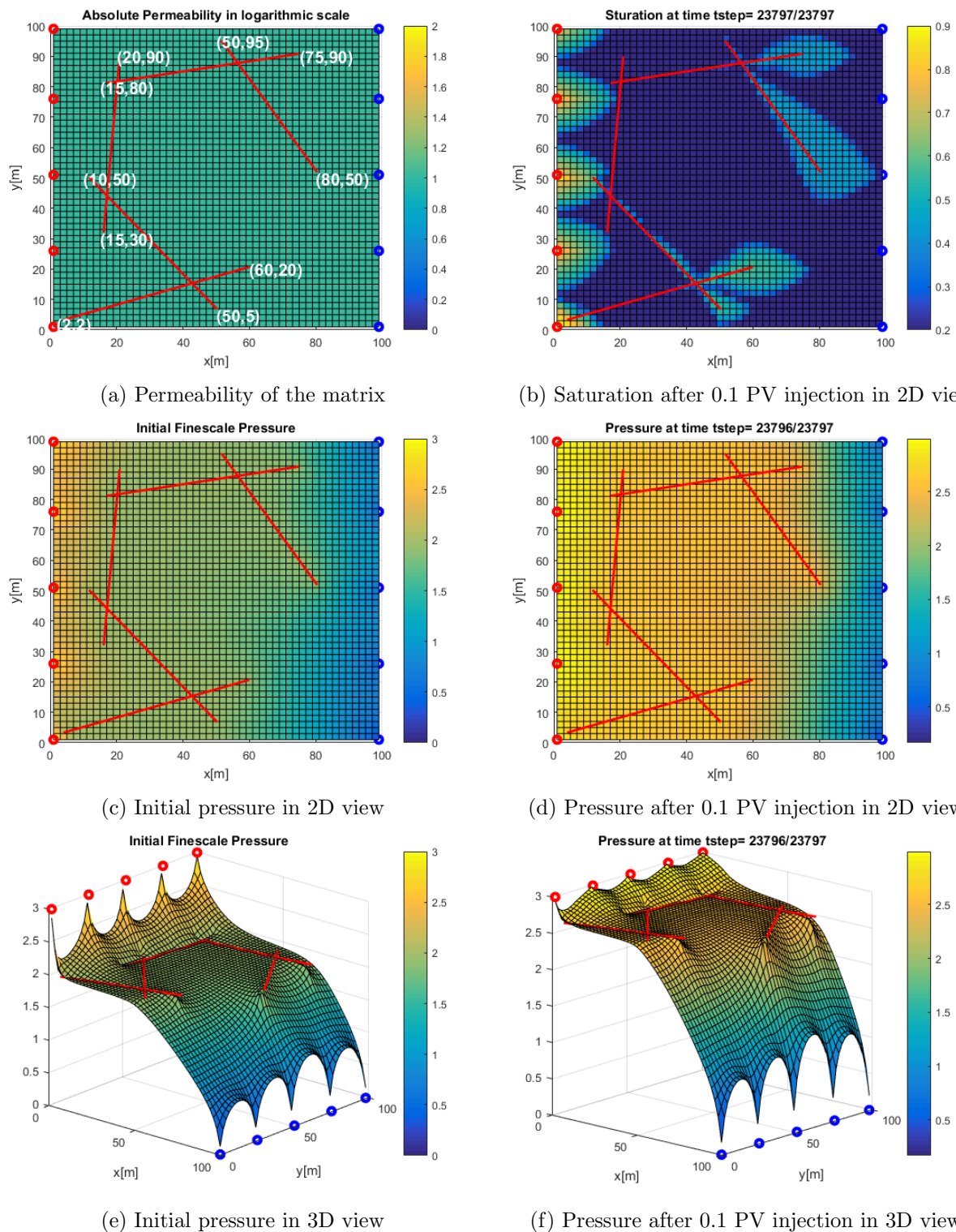


Figure 2.10: Results of test case 4: a complex fracture network spanning most of the reservoir is being modeled by EDFM. Note the effect of fracture in flow and transport is quite significant, leading to early water break through.

Chapter 3

Multiscale Finite Volume Method for Fractured Porous Media (F-MSFV)

In this chapter, MSFV for fractured porous media (F-MSFV) is revisited. Such a revisit is important in order to develop the multilevel multiscale method. Like many advanced computational methods, MSFV requires its own computational grids which are imposed on the given fine-scale grid. MSFV, in particular, imposes two sets of coarse grids, namely: primal coarse (coarse from now on) and dual-coarse grids. Next we explain the construction of these sets of grid cells.

3.1. MSFV Grids

On the given fine-scale grid, the primal coarse grid is imposed. Primal coarse cells form a non-overlapping partitioning of the computational domain, with flexible geometry and resolution (i.e., arbitrary coarsening factor in each direction). A selected fine-grid cell in each coarse grid cell is taken as the coarse node (or vertex). The solution at coarse nodes will be found by solving the coarse-scale system. By connecting the coarse nodes, a secondary –i.e., dual– coarse grid is obtained. As shown in Fig. 3.1, for 2D structured rectangular grids, each dual-coarse cell has four coarse nodes in its corners. For fractured media, using EDFM, sets of primal and dual coarse cells are obtained for both matrix and fracture domains. This is illustrated in Figs. 3.2 and 3.3. Note that, as Fig. 3.1 also illustrates, the fine-scale grid cells can be flagged based on their positions with respect to the dual-coarse grid: Vertex (coarse nodes), Edge (at the edge of dual-coarse cells), and Interior (inside dual-coarse cells).

Next, the F-MSFV formulation is explained.

3.2. F-MSFV Formulation

Let us recall the EDFM pressure equation for a fractured medium, i.e.,

$$-\nabla \cdot (\lambda_t \cdot \nabla p)^m = \eta^m (p^f - p^m) + \xi^m (p^w - p^m), \quad (3.2.1)$$

and

$$-\nabla \cdot (\lambda_t \cdot \nabla p)^f = \eta^f (p^m - p^f) + \xi^f (p^w - p^f), \quad (3.2.2)$$

where $\int_V \eta^m dv = \int_A \eta^f dS = CI \lambda_t$, $\int_V \xi^m dv = PI \lambda_t$, and $\int_A \xi^f dS = PI \lambda_t$ with PI being the well (injector or producer) productivity index [34].

Instead of solving for the matrix and fracture pressures at fine-scale resolution, i.e., p^m and p^f , the F-MSFV provides an approximated pressure p' by superposition of coarse-scale solution \check{p} with

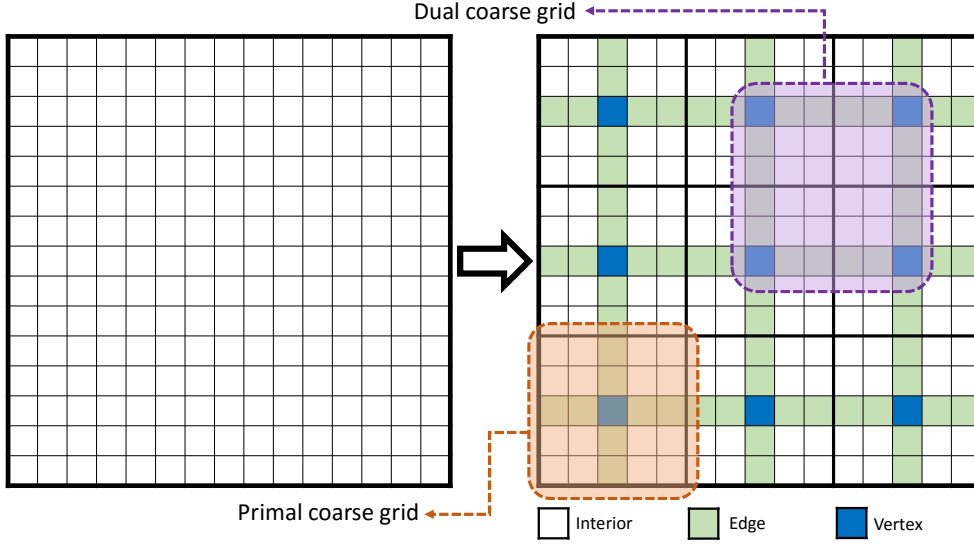


Figure 3.1: Construction of primal and dual coarse grid structure in multiscale approach for a 2D sample with 15×15 of fine grids. This sample is divided into 3×3 primal coarse grids. The coarsening ratio here is 5.

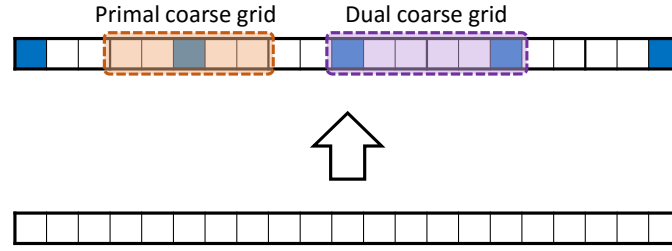


Figure 3.2: Construction of primal and dual coarse grids for fracture. In this example, fracture has 21 elements and is divided into 5 unequal primal coarse grids. The coarsening ratio here is 5.

using locally calculated "basis functions" [1], i.e.,

$$p^m \approx p'^m = \sum_{i=1}^{N_{cm}} \Phi_i^{mm} \check{p}_i^m + \sum_{i=1}^{N_f} \sum_{j=1}^{N_{cf_i}} \Phi_j^{mf_i} \check{p}_j^{f_i} + \sum_{k=1}^{N_w} \Phi_k^{mw} \check{p}_k^w \quad (3.2.3)$$

for the matrix, and

$$p^f \approx p'^f = \sum_{i=1}^{N_{cm}} \Phi_i^{fm} \check{p}_i^m + \sum_{i=1}^{N_f} \sum_{j=1}^{N_{cf_i}} \Phi_j^{ff_i} \check{p}_j^{f_i} + \sum_{k=1}^{N_w} \Phi_k^{fw} \check{p}_k^w \quad (3.2.4)$$

for the fractures, respectively. Here, Φ^{mm} , Φ^{mf} and Φ^{mw} are the components of matrix basis function for each matrix coarse node taking the matrix-fracture (Φ^{mf}) and matrix-well interactions (Φ^{mw}) in the matrix into account. Similarly, Φ^{fm} , Φ^{ff} and Φ^{fw} together form the fracture basis functions for each fracture coarse node. Next, the computation of the local basis functions is explained.

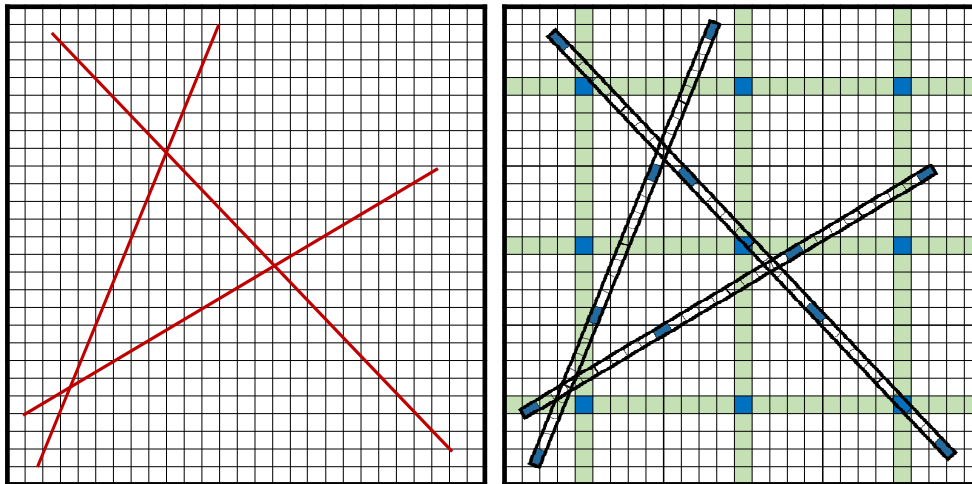


Figure 3.3: Construction of coarse grids for 2D fractured media. Coarsening ratio is 9.

3.3. Basis Functions

Basis functions are local solutions of the governing equations without right-hand-side (RHS) terms on dual-coarse cells, subject to local boundary conditions. The constructions of basis functions for matrix and fracture domains are briefly explained in this chapter. Note that the full description can be found in the recently published MSFV for fractured media (F-AMS) [1]. More precisely, what follows is the Frac-AMS approach presented in the literature [1], in which the matrix basis functions have the presence of the fractures taken into account, but fracture basis functions are just 1D interpolations inside the fractures with no matrix effects being present. The Frac-AMS approach allows for capturing the effect of fractures in the matrix domain, while the pressure distribution in fractures are interpolated much simpler.

The mathematical formulation for matrix and fracture basis functions, using Frac-AMS approach [1], reads

$$-\nabla \cdot (\lambda_t^m \cdot \nabla \Phi^m) - \eta^m (\Phi^f - \Phi^m) - \xi^m (\Phi^w - \Phi^m) = 0, \quad (3.3.1)$$

$$-\nabla \cdot (\lambda_t^f \cdot \nabla \Phi^{ff}) = 0 \quad (3.3.2)$$

where Φ^m clusters all the individual Φ^{mm} , Φ^{mf} , and Φ^{mw} . Note that similar to F-AMS [1], in this work, well basis functions are set to unit 1, i.e., $\Phi^w = 1$, and again $\Phi^{fm} = \Phi^{fw} = 0$ due to Frac-AMS coupling approach [1].

The procedure to solve for the sets of basis function equations is quite straightforward. Let us consider basis function corresponding to coarse node x_k in the matrix. The basis functions corresponding to this node are solved by setting the solution at this coarse node to 1, i.e., $\Phi(x_k) = 1$ and at all other coarse nodes (in matrix and fractures) to 0. If the node is inside fractures, due to their 1D geometry in our work, the fracture basis functions are solved directly. If the node is inside matrix, then one solves reduced-dimensional boundary condition [23, 35] on the edges of the dual-coarse cells inside matrix (note that fracture basis functions are Dirichlet condition for the matrix basis functions). Then the edge and coarse-node solutions serve as Dirichlet boundary condition for the interior cells of dual-coarse blocks [1].

Figure 3.5 shows an example of a matrix basis function for the domain corresponding to Fig. 3.3, when no fracture neither wells overlap with the local support region. Note that the basis function represent the heterogeneity of the local support, and that the only assumption in their calculation is the imposed reduced-dimensional localization condition [35].

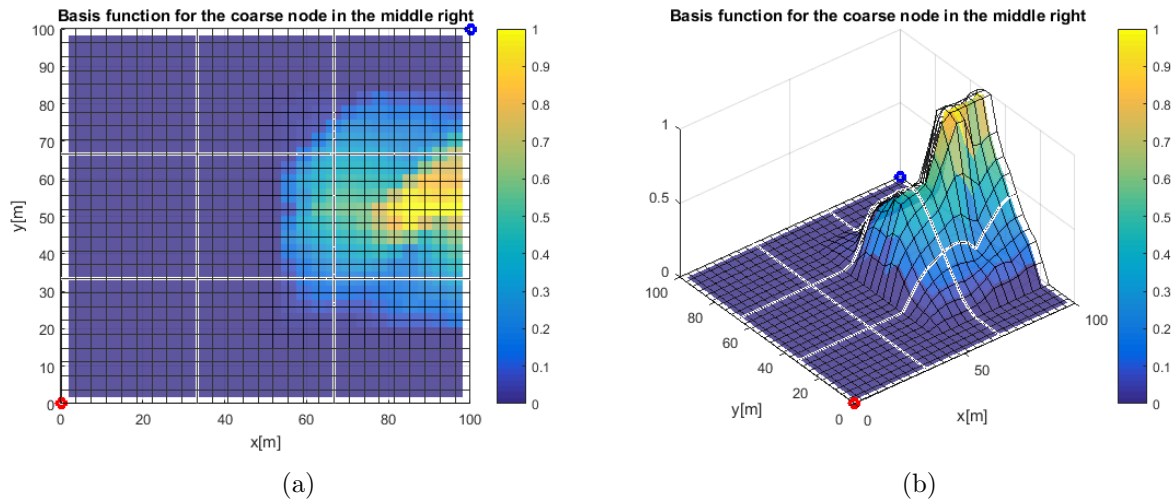
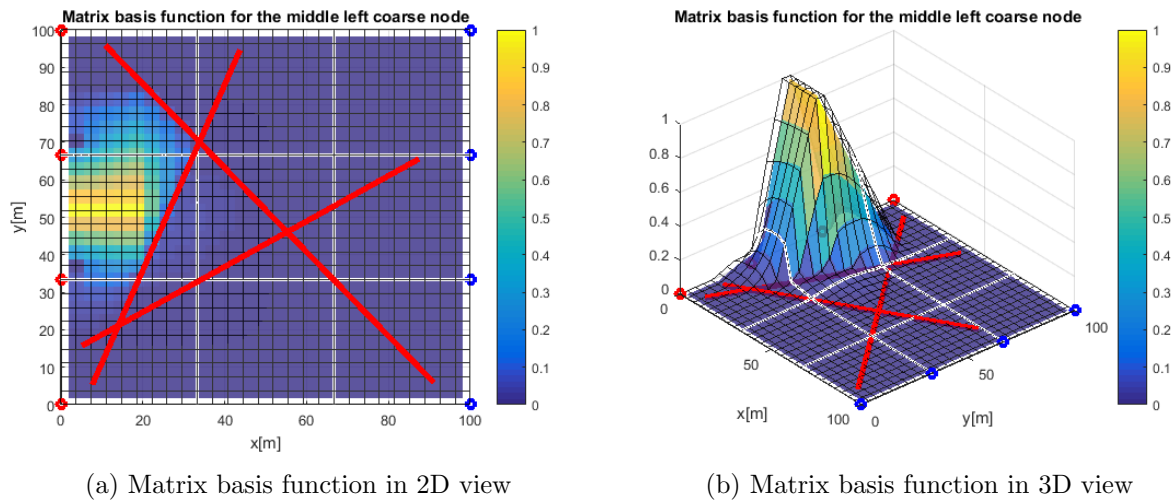


Figure 3.4: Local basis function (without any fracture) for the coarse node (3, 2) in 2D (left) and 3D (right) view, for a heterogeneous test case. The white lines are the boundaries of primal coarse grids.

Now adding fractures, the basis functions would capture the heterogeneity and fractures and wells. The effect of having overlapping fractures is illustrated in the plots provided in Figs. 3.5 and 3.6.



(a) Matrix basis function in 2D view

(b) Matrix basis function in 3D view

Figure 3.5: A matrix basis function for the sample shown in figure 3.3.

In addition, the presented formulation for basis functions allow the matrix domain capture the effect of (injection or production) wells through Φ^{mw} . Without taking well effects into account, the matrix basis functions would only capture the heterogeneity, as seen in Fig. 3.7. However, our formulation does capture the well effect, as shown in Figs. 3.8 and 3.9.

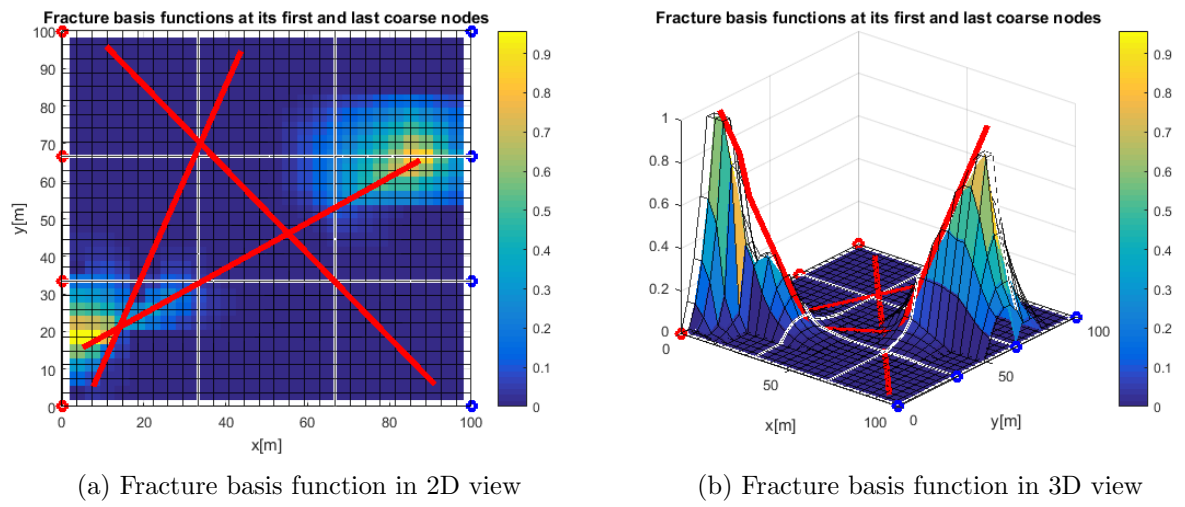


Figure 3.6: Fracture basis functions at first and last coarse nodes of one fracture for the sample shown in figure 3.3.

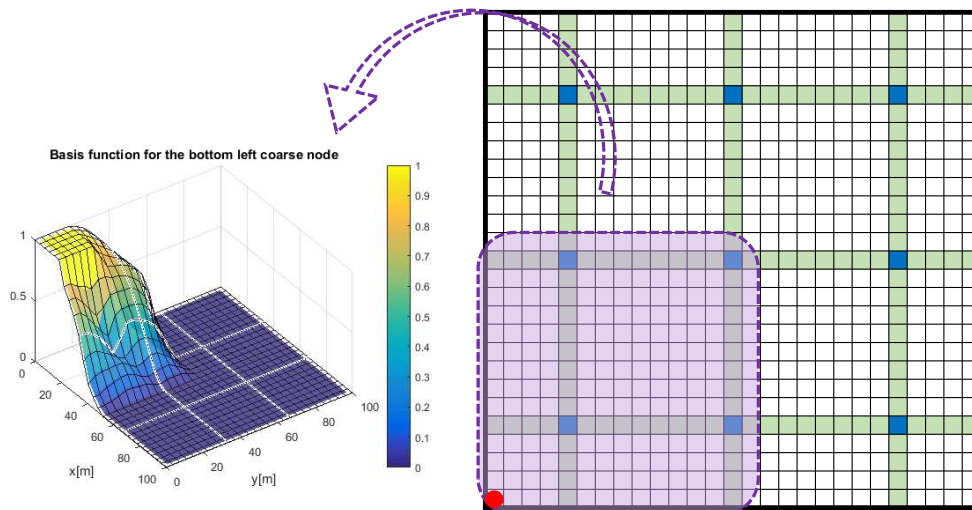


Figure 3.7: An example of basis function without capturing the effect of well located in the corner.

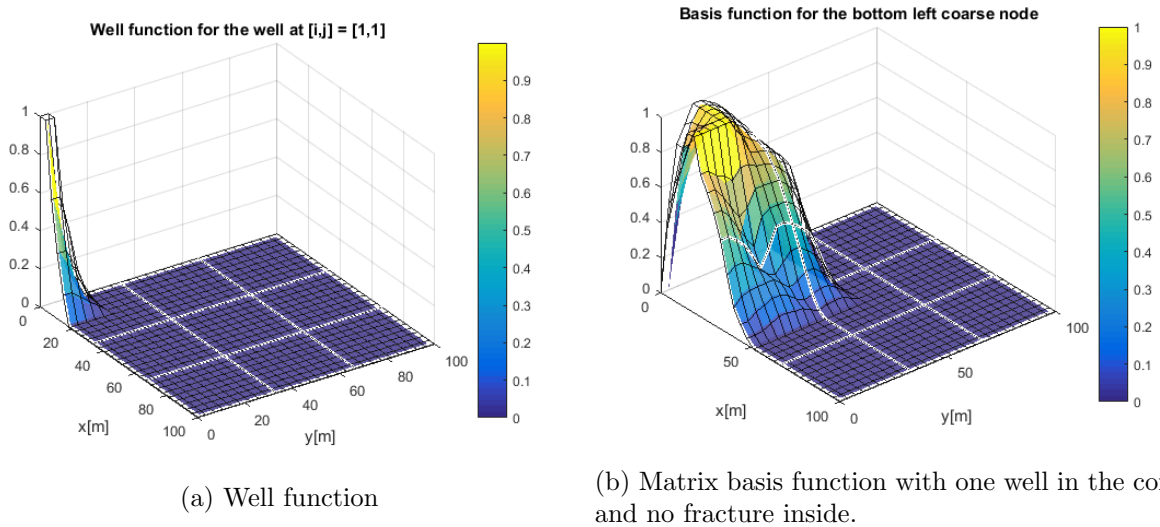


Figure 3.8: Figure (b) shows the basis function of the highlighted assemble dual coarse region of the 27×27 sample with one well in the corner which is now seen as pressure drop. Figure (a) is the well function of the corresponding well.

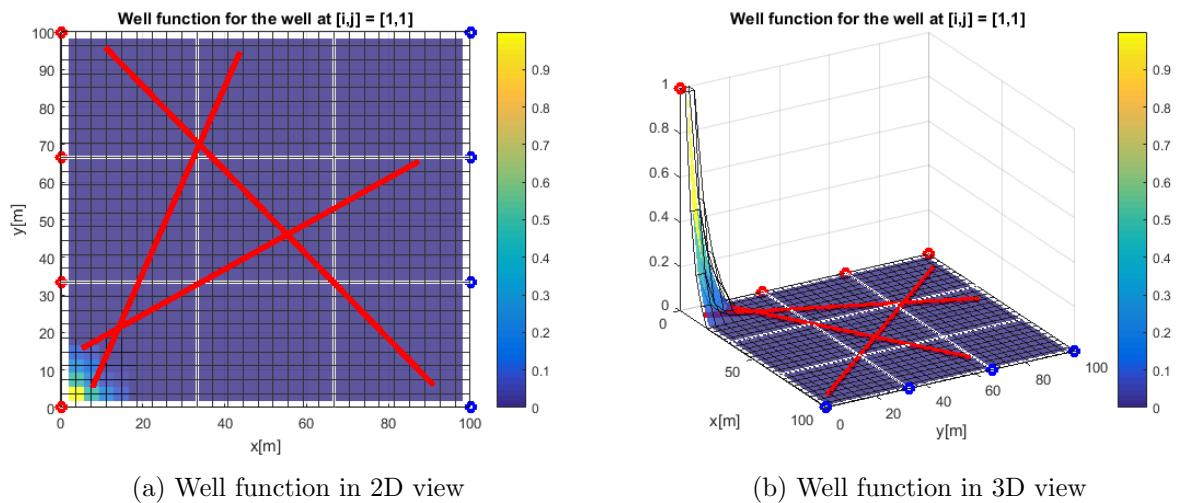


Figure 3.9: Well function containing fracture inside its domain of the well located at $[i, j] = [1, 1]$ for the sample shown in figure 3.3.

3.3.1. Algebraic Form of Basis Functions (Prolongation Operator)

It is crucial for further development of this work, i.e., multilevel multiscale formulation, to write multiscale formulation in matrix-vector –i.e., algebraic– notation. This requires one to define the operator of basis functions –i.e., Prolongation operator \mathcal{P} – which clusters all basis functions into its columns, i.e.,

$$P_{(N \times N_c)} = \begin{array}{c} \begin{array}{cccccccc} \Phi_1 & \Phi_2 & \Phi_3 & \Phi_4 & \cdots & \Phi_{N_c-1} & \Phi_{N_c} \\ \downarrow & \downarrow & \downarrow & \downarrow & & \downarrow & \downarrow \end{array} \\ \begin{bmatrix} | & 0 & 0 & 0 & \cdots & 0 & 0 \\ | & \vdots & 0 & | & \cdots & 0 & 0 \\ \vdots & 0 & 0 & | & \cdots & 0 & 0 \\ | & | & \vdots & | & \cdots & \vdots & 0 \\ 0 & | & | & \vdots & \cdots & | & \vdots \\ \vdots & \vdots & | & 0 & \cdots & | & | \\ 0 & 0 & \vdots & 0 & \cdots & \vdots & | \\ 0 & 0 & 0 & 0 & \cdots & 0 & | \end{bmatrix}, \quad \check{p} = \begin{bmatrix} \check{p}_1 \\ \check{p}_2 \\ \check{p}_3 \\ \vdots \\ \vdots \\ \check{p}_{N-1} \\ \check{p}_N \end{bmatrix} \end{array} \quad (3.3.3)$$

This allows for representation of the rest of the F-MSFV algorithm in much simpler way. Now that the basis functions are computed and the Prolongation operator is constructed, one has to construct and solve the coarse-scale system. This will be explained in the next subsection. Having p_c solved (to be explained in the next subsection), the multiscale approximation for pressure – algebraically– reads

$$p \approx p' = \mathcal{P} p_c. \quad (3.3.4)$$

3.4. Coarse-scale system

The pressure equation for EDFM fractured system can be written algebraically as

$$Ap = q, \quad (3.4.1)$$

where $p = [p^m \ p^f \ p^w]^T$ and q contains all RHS terms for the corresponding subdomains (matrix, fractured and wells). Similarly, A clusters all the matrix, fracture, and well transmissibility and coupling terms.

To construct the coarse-scale system, one has to define a Restriction operator \mathcal{R} , which –opposite of Prolongation– maps the solution from fine to coarse scale. There are two classes of Restriction operator, Finite-Volume (FV) and Finite-Element (FE) methods. In this work, due to the crucial importance of local mass conservation, the FV-based Restriction operator is followed. The entries of the restriction operator r_{ij} are obtained as

$$r_{ij} = \begin{cases} 1 & \text{if } x(j) \in \Omega_i \\ 0 & \text{otherwise} \end{cases} \quad (3.4.2)$$

Using the restriction and prolongation operator, after some mathematical manipulations, one obtains the coarse-scale linear system as

$$\underbrace{(\mathcal{R}\mathcal{A}\mathcal{P})}_{A_c} \underbrace{p_c}_{\mathcal{R}p} = \underbrace{\mathcal{R}q}_{q_c}. \quad (3.4.3)$$

By solving the coarse-scale system for p_c , the approximate fine-scale solution p' is obtained via the superposition expression. Finally, the whole multiscale procedure can be summarized in the following expression, i.e.,

$$p' = \mathcal{P}(\mathcal{R}A\mathcal{P})\mathcal{R} p. \quad (3.4.4)$$

As the only source of error in F-MSFV basis algorithm for matrix domain is in the localization assumption, the residual of the F-MSFV solution p' in fulfillment of the fine-scale reference system, i.e., $A p' - q$, is non-zero only at the dual-coarse cell boundary (edge) cells [35]. Next, before proceeding with the development of multilevel multiscale method, to illustrate the F-MSFV results of the developed MATLAB simulator of this thesis work, some results are presented.

3.5. Results and Validation

The Frac-AMS strategy was implemented in MATLAB for 2D fractured porous media. For the parameters used identically in all test cases, please see table 2.1. At all cases, the fractures permeability is 10^5 times larger than the maximum permeability of matrix. Moreover, in all the results, second-norm error is calculated by comparing the multiscale pressure with reference pressure which is the pressure solution at fine-scale, i.e.,

$$Err_{norm} = \frac{\| p_{ms} - p_{fs} \|_2}{\| p_{fs} \|_2}, \quad (3.5.1)$$

where $\| p_{ms} - p_{fs} \|_2 = \sqrt{\sum_{i=1}^{N_f} [p_{ms_i} - p_{fs_i}]^2}$, and $\| p_{fs} \|_2 = \sqrt{\sum_{i=1}^{N_f} [p_{fs_i}]^2}$.

p_{fs_i} and p_{ms_i} are the finescale and (approximated) multiscale pressure solutions at cell i (either in the matrix or the fractures) respectively.

Moreover, the multiscale pressure graph consists of an absolute error curve underneath the pressure curve which is simply calculated as $Error = | p_{fs} - p_{ms} |$. This error is not the normalized error and it is present just to illustrate the differences between finescale and multiscale pressure through the domain. All results include residual surface plot in fulfillment of fine-scale equation. Note that non-zero terms in residual exist at the boundaries of dual coarse cells (which is the indication of the correctness of the developed simulator).

3.5.1. Test Case 1: Quarter of Five Spot with no fracture

This test case consists of a 77×77 homogeneous sample with one injection well at bottom left corner and one production well at top right corner. The coarsening ratio here is 11. The result with comparison of multiscale with the reference (finescale) solution are shown in figure 3.10.

3.5.2. Test Case 2: Quarter of Five Spot with One Diagonal Fracture

One fracture lies diagonally in a homogeneous matrix with one injection well at bottom left corner and one production well at top right corner. Test case consists of $77 \times 77 = 5929$ matrix cells and 36 fracture elements. The coarsening ratio is 7.

3.5.3. Test Case 3: Line drive with Two Fractures Perpendicular to each other, "+" Shape (fractures on the boundaries of primal coarse grids)

Two fractures perpendicular to each other (horizontal and vertical) in a homogeneous matrix with line drive of 5 injection wells at the left boundary and 5 production wells at the right boundary. Test case consists of $60 \times 60 = 3600$ matrix cells and 92 fracture elements. Coarsening ratio is 15. Note that the gridding is chosen in such a way that fractures are located on the boundaries of primal coarse grids.

3.5.4. Test Case 4: Line drive with Two Fractures Perpendicular to each other, ”+” Shape (fractures on the boundaries of dual coarse grids)

Two fractures perpendicular to each other (horizontal and vertical) in a homogeneous matrix with line drive of 5 injection wells at the left boundary and 5 production wells at the right boundary. Test case consists of $75 \times 75 = 3600$ matrix cells and 92 fracture elements. Coarsening ratio is 15. Note here that opposite to the previous test case, the gridding is chosen in such a way that fractures are now located on the boundaries of dual coarse grids.

3.5.5. Test Case 5: Line drive with Two Diagonal Fractures Perpendicular to each other, ”x” Shape

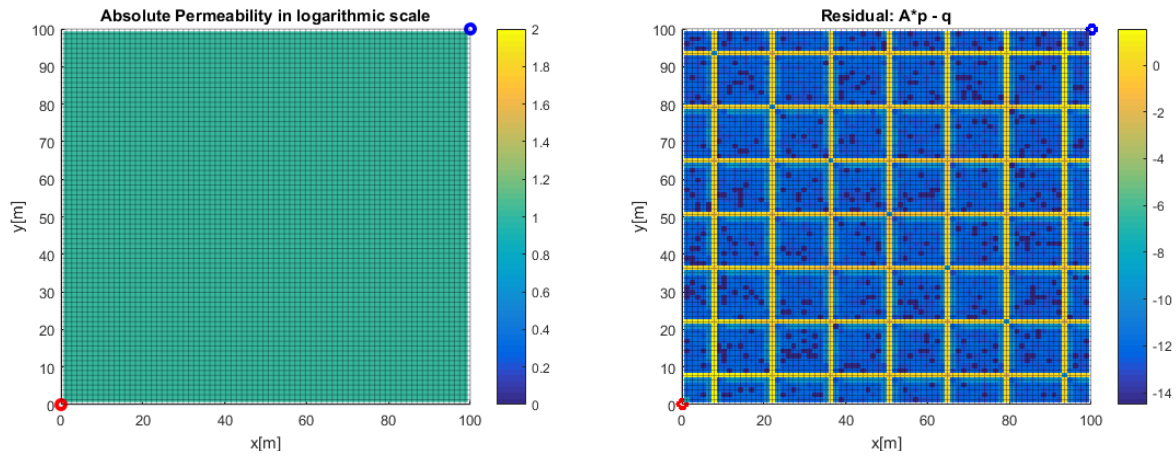
Two diagonal fractures perpendicular to each other in a heterogeneous matrix with line drive of 4 injection wells at the left boundary and 4 production wells at the right boundary. Test case consists of $91 \times 91 = 8281$ matrix cells and total number of 106 fracture elements. Coarsening ratio is 13. Permeability contrast of matrix is $k_{max}/k_{min} = 2.2 \times 10^4$.

3.5.6. Test Case 6: Line drive with 5 Random Fractures

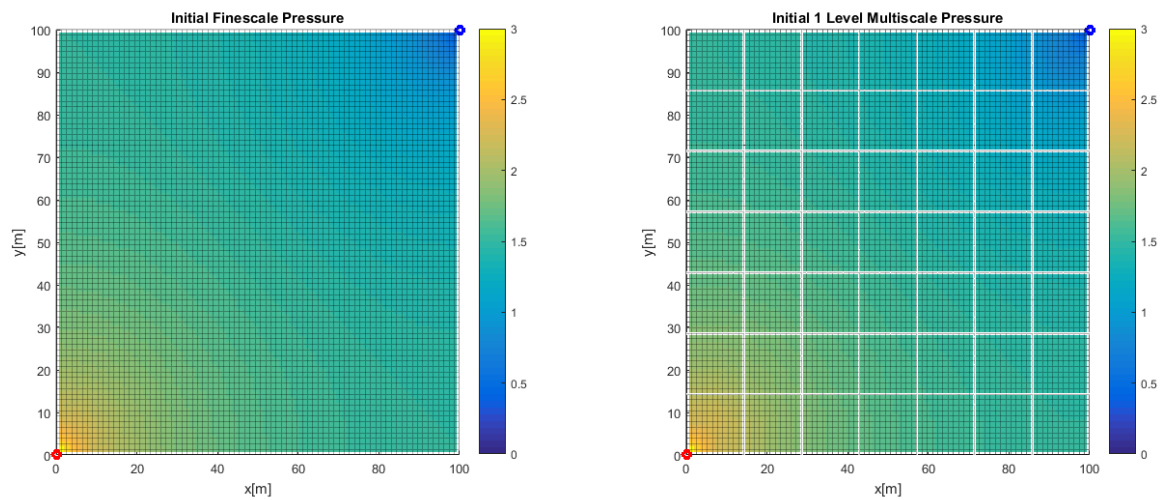
Five fractures in a heterogeneous matrix with line drive of 5 injection wells at the left boundary and 5 production wells at the right boundary. Test case consists of $99 \times 99 = 9801$ matrix cells and total number of 247 fracture elements. Coarsening ratio is 11. Permeability contrast of matrix is $k_{max}/k_{min} = 2.0 \times 10^4$.

3.6. Discussion

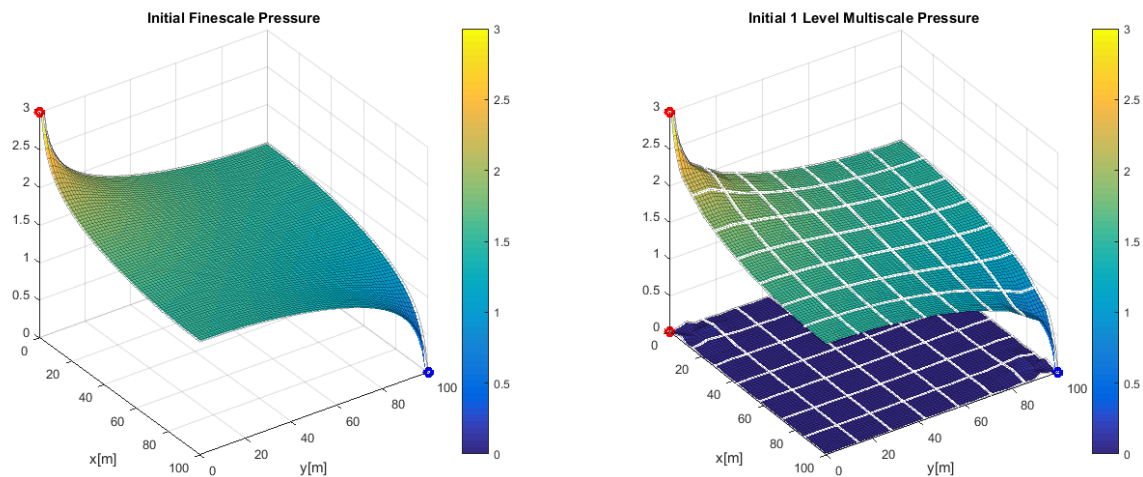
The implemented F-MSFV simulator, following Frac-AMS approach, resulted in an acceptable approximation of the fine-scale pressure for many challenging test cases. Residual plots confirm the correctness of the developed MATLAB simulator, allowing us to proceed with development of the novel multilevel multiscale method of this thesis work. Note that the F-MSFV is found sensitive to the coarsening ratio (for both matrix and fracture), and the heterogeneity contrasts. The accuracy of the F-MSFV solutions can be systematically improved through iterative procedure, which was first developed in [32] and later extended in [19, 28, 1].



(a) Permeability of the matrix

(b) Residual ($Ap - q$)

(c) Finescale (left) and multiscale (right) pressure in 2D view.



(d) Finescale (left) and multiscale (right) pressure in 3D view.

Figure 3.10: Results of test case 1: a) homogeneous permeability plot in logarithmic scale with well positioning. b) residual ($Ap - q$) plot in logarithmic scale indicating non-zero values at dual coarse cell boundaries. c,d) pressure solution in 2D and 3D views. The graphs at left show the fine-scale pressure result (solved with 77×77 cells) where the graphs at right show multiscale pressure result (solved by 7×7 coarse cells) with significantly less number of DOFs. The coarsening ratio here is 11. The white lines indicate the boundaries of primal coarse grids. The plotted graph below the 3D multiscale graph in the right figure is the difference between fine-scale and multiscale solution. The normalized error is $\frac{\|p_{ms} - p_{fs}\|_2}{\|p_{fs}\|_2} = 8.24 \times 10^{-3}$.

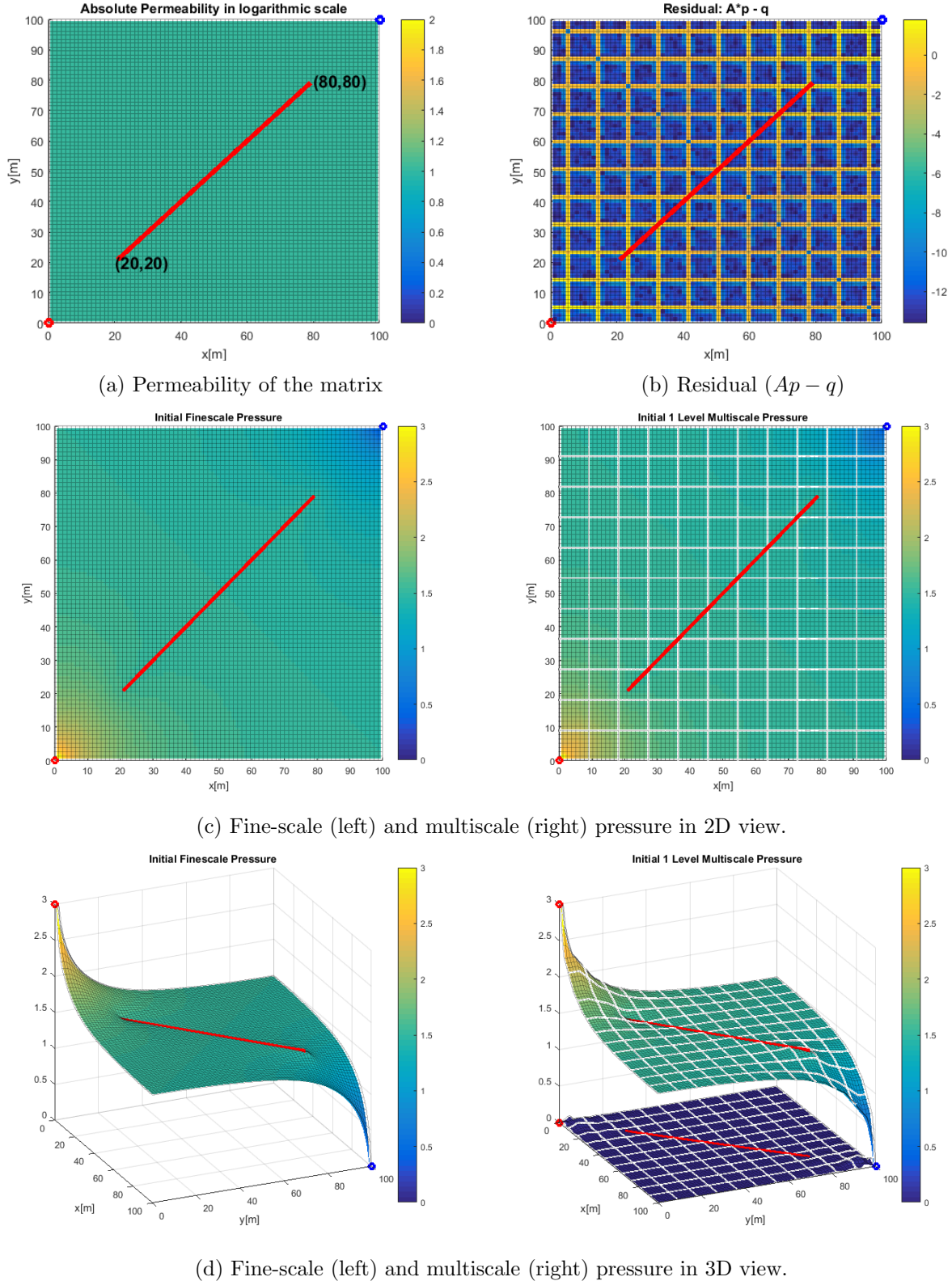


Figure 3.11: Results of test case 2: a) heterogeneous permeability plot in logarithmic scale with fracture and well positioning. b) residual ($Ap - q$) plot in logarithmic scale indicating non-zero values at dual coarse cell boundaries. c,d) pressure solution in 2D and 3D views. The graphs at left show the fine-scale pressure result (solved with 77×77 matrix cells and 36 fracture elements) where the graphs at right show multiscale pressure result (solved by 11×11 matrix coarse cells and 6 fracture course cells) with significantly less number of DOFs. The coarsening ratio here is 7. The white lines indicate the boundaries of primal coarse grids. The plotted graph below the 3D multiscale graph in the right figure is the difference between fine-scale and multiscale solution. The normalized error is $\frac{\|p_{ms} - p_{fs}\|_2}{\|p_{fs}\|_2} = 6.65 \times 10^{-3}$.

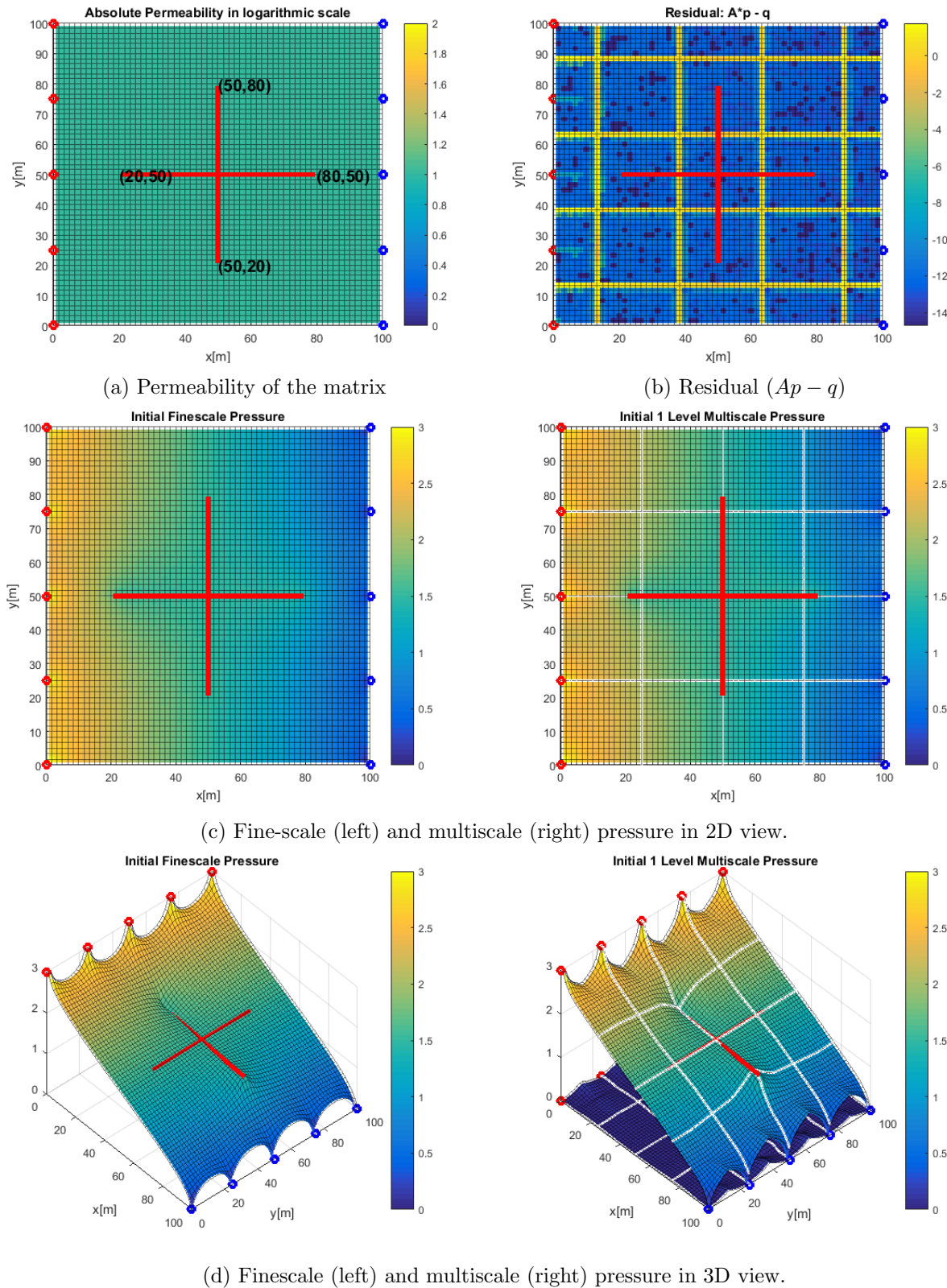


Figure 3.12: Results of test case 3: a) homogeneous permeability plot in logarithmic scale with fracture and well positioning. b) residual ($Ap - q$) plot in logarithmic scale indicating non-zero values at dual coarse cell boundaries. c,d) pressure solution in 2D and 3D views. The graphs at left show the fine-scale pressure result (solved with 60×60 matrix cells and 92 fracture elements) where the graphs at right show multiscale pressure result (solved by 4×4 matrix coarse cells and 8 fracture course cells) with significantly less number of DOFs. The coarsening ratio here is 15. The white lines indicate the boundaries of primal coarse grids. The plotted graph below the 3D multiscale graph in the right figure is the difference between fine-scale and multiscale solution. The normalized error is $\frac{\|p_{ms} - p_{fs}\|_2}{\|p_{fs}\|_2} = 2.34 \times 10^{-2}$.

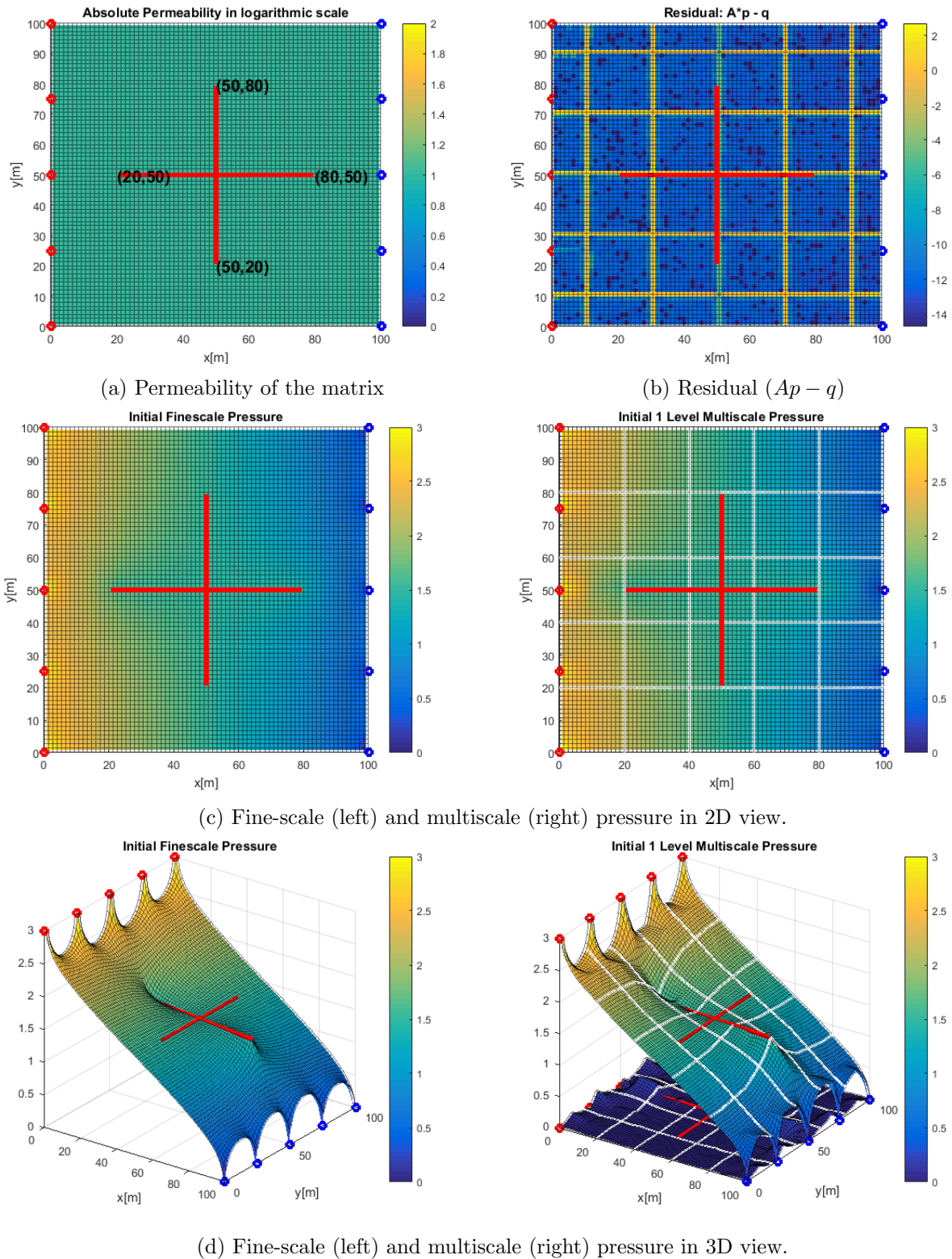


Figure 3.13: Results of test case 4: a) homogeneous permeability plot in logarithmic scale with fracture and well positioning. b) residual ($Ap - q$) plot in logarithmic scale indicating non-zero values at dual coarse cell boundaries. c,d) pressure solution in 2D and 3D views. The graphs at left show the fine-scale pressure result (solved with 75×75 matrix cells and 92 fracture elements) where the graphs at right show multiscale pressure result (solved by 5×5 matrix coarse cells and 8 fracture course cells) with significantly less number of DOFs. The coarsening ratio here is 15. The white lines indicate the boundaries of primal coarse grids. The plotted graph below the 3D multiscale graph in the right figure is the difference between fine-scale and multiscale solution. The normalized error is $\frac{\|p_{ms} - p_{fs}\|_2}{\|p_{fs}\|_2} = 2.66 \times 10^{-2}$.

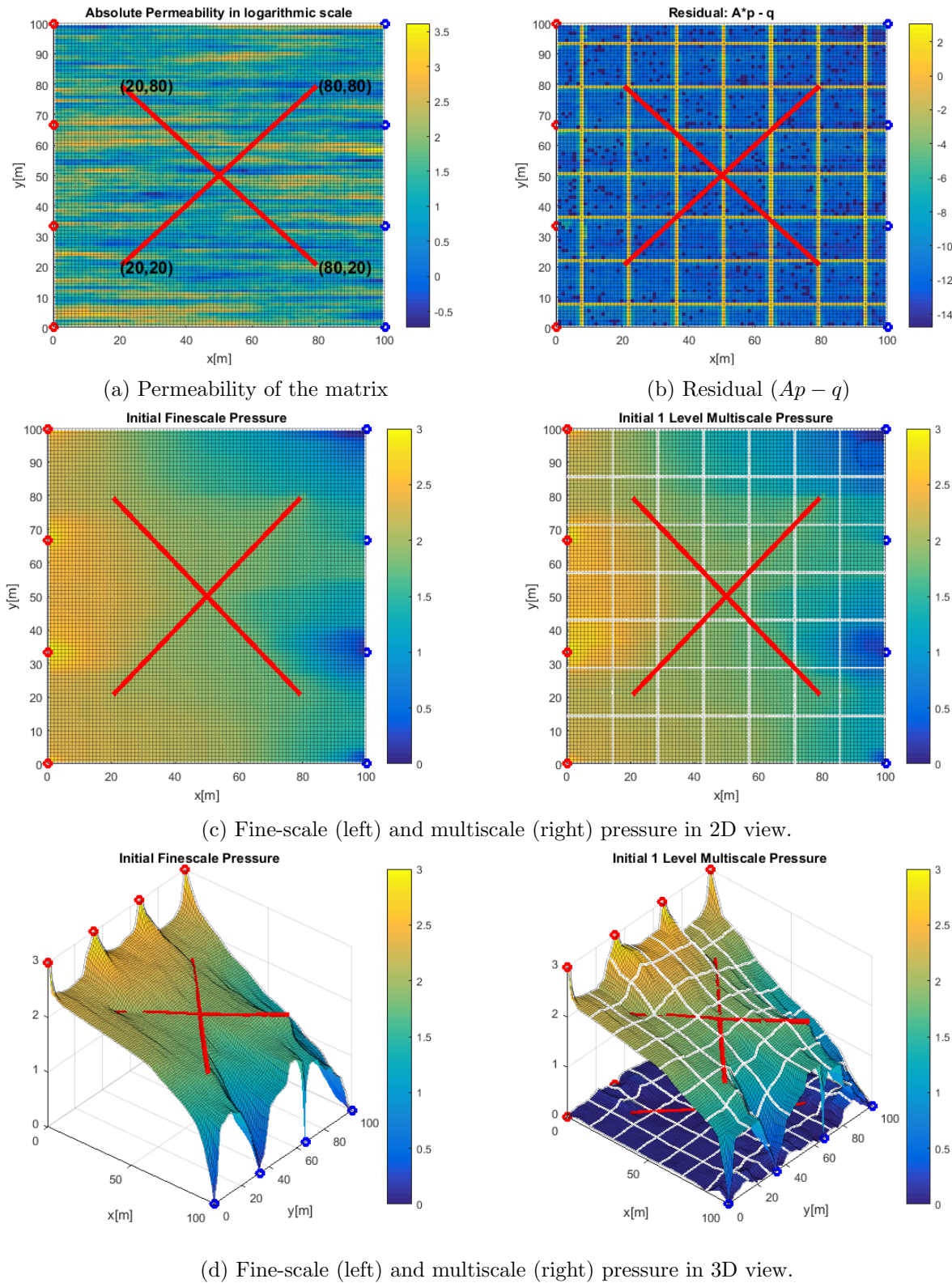


Figure 3.14: Results of test case 5: a) heterogeneous permeability plot in logarithmic scale with fracture and well positioning. b) residual ($Ap - q$) plot in logarithmic scale indicating non-zero values at dual coarse cell boundaries. c,d) pressure solution in 2D and 3D views. The graphs at left show the fine-scale pressure result (solved with 91×91 matrix cells and 106 fracture elements) where the graphs at right show multiscale pressure result (solved by 7×7 matrix coarse cells and 10 fracture course cells) with significantly less number of DOFs. The coarsening ratio here is 13. The white lines indicate the boundaries of primal coarse grids. The plotted graph below the 3D multiscale graph in the right figure is the difference between fine-scale and multiscale solution. The normalized error is $\frac{\|p_{ms} - p_{fs}\|_2}{\|p_{fs}\|_2} = 5.58 \times 10^{-2}$.

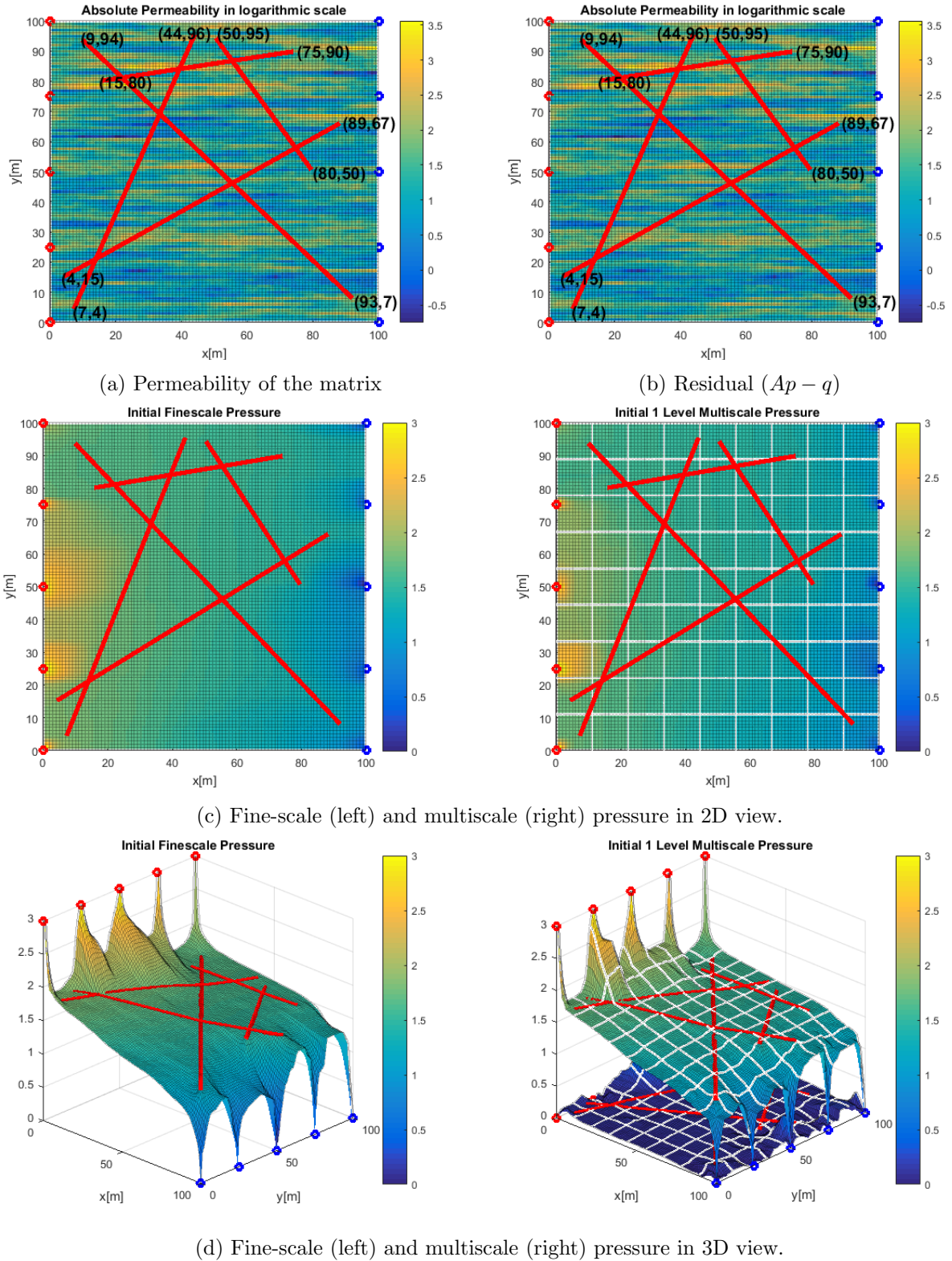


Figure 3.15: Results of test case 6: a) heterogeneous permeability plot in logarithmic scale with fracture and well positioning. b) residual ($Ap - q$) plot in logarithmic scale indicating non-zero values at dual coarse cell boundaries. c,d) pressure solution in 2D and 3D views. The graphs at left show the fine-scale pressure result (solved with 99×99 matrix cells and 247 fracture elements) where the graphs at right show multiscale pressure result (solved by 9×9 matrix coarse cells and 27 fracture course cells) with significantly less number of DOFs. The coarsening ratio here is 11. The white lines indicate the boundaries of primal coarse grids. The plotted graph below the 3D multiscale graph in the right figure is the difference between fine-scale and multiscale solution. The normalized error is $\frac{\|p_{ms} - p_{fs}\|_2}{\|p_{fs}\|_2} = 7.22 \times 10^{-2}$.

Chapter 4

Multilevel Multiscale Method for Embedded Discrete Fracture Model (F-MLMS)

F-MLMS is presented in this chapter. First, the multilevel multiscale (MLMS) method is introduced for non-fractured media, then, the extension to include explicit fractures at multiple coarse resolutions is being introduced. This chapter focuses on method development, and the next chapter results are presented.

4.1. MultiLevel MultiScale Finite Volume Method (MLMS)

In chapter 3, it was shown that multiscale method provides efficient solution for flow in heterogeneous media, by solving the problem at the coarse scale while honoring heterogeneity at the original fine scale. The coarse-scale solution is interpolated back to the original fine-scale resolution, which is a unique advantage compared with upscaling methods. What presented above was only for 1 level of coarsening. Now, in this thesis, we extend the multiscale formulation to include multiple levels of accurate coarsening and refining. This would be a significant achievement for real-field applications.

4.1.1. MLMS Formulation

Let us consider the elliptic pressure equation, i.e.,

$$-\nabla \cdot (\lambda_t \cdot \nabla p) = q_t. \quad (4.1.1)$$

As discussed in the previous chapter, the approximate multiscale solution p' is obtained via the superposition expression which reads

$$p \approx p' = \sum_{k=1}^{N_{c_1}} \Phi_k^{c_1} p_k^{c_1}, \quad (4.1.2)$$

where N_{c_1} and Φ^{c_1} are the number of coarse cells and basis functions. Moreover, p^{c_1} is the coarse-scale solution. Now, to extend it to a multilevel formulation, one can consider the first-level coarse solution p^{c_1} as a fine-scale solution for the second level of coarse resolution. This would allow to naturally extend the superposition expression as

$$p^{c_1} = \sum_{l=1}^{N_{c_2}} \Phi_l^{c_2} p_l^{c_2}, \quad (4.1.3)$$

where, N_{c_2} and Φ^{c_2} are, respectively, the number of second-level coarse cells and the second-level basis functions, Moreover, p^{c_2} is the second-level coarse solution. As such, one can finally obtain

$$p \approx p' = \sum_{k=1}^{N_{c_1}} \left(\Phi_k^{c_1} \left[\sum_{l=1}^{N_{c_2}} \Phi_l^{c_2} p_l^{c_2} \right]_k \right), \quad (4.1.4)$$

which allows for construction of the two-level coarse system as

$$-\nabla \cdot \left(\lambda_t \cdot \nabla \sum_{k=1}^{N_{c_1}} \left(\Phi_k^{c_1} \left[\sum_{l=1}^{N_{c_2}} \Phi_l^{c_2} p_l^{c_2} \right]_k \right) \right) = q_t. \quad (4.1.5)$$

4.1.2. MLMS Coarse Grid Construction

The coarse grid structure at first coarsening level of MLMS is the same as in MSFV. The second level coarse grids are then constructed on top of the coarse grids at previous level as if the coarse grids of coarsening level 1 is considered as a fine-scale grid system and the same procedure in MSFV coarse grid construction is applied. Figure 4.1 shows an example of coarse grid construction for a two-level multiscale sample.

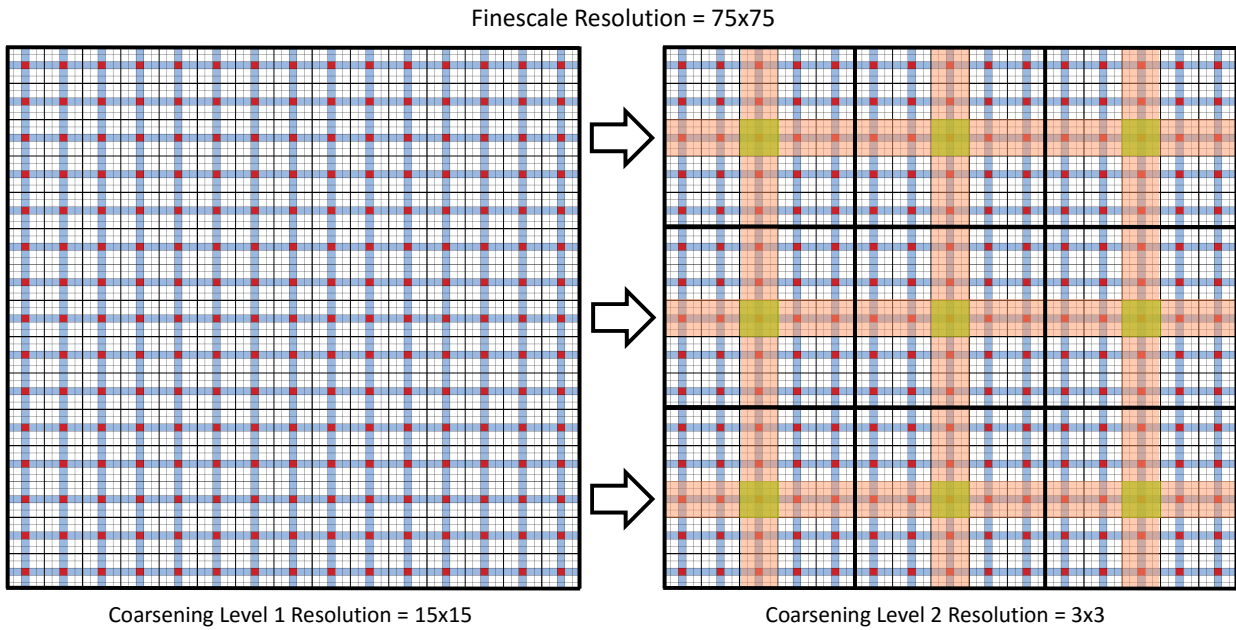


Figure 4.1: Construction of primal and dual coarse grids for a 1-level (left) and 2-level (right) MLMS method. The coarsening ratio here is 5 for both two multiscale levels.

4.1.3. MLMS Prolongation and Restriction Operators

Based on description of prolongation and restriction operators at section 3.3.1, the equation for coarsening level 1 in matrix-vector form reads:

$$\mathcal{R}_{(N_{c_1} \times N_f)}^{c_1 f} A_{(N_f \times N_f)}^f \left[\mathcal{P}_{(N_f \times N_{c_1})}^{f c_1} p_{(N_{c_1} \times 1)}^{c_1} \right] = \mathcal{R}_{(N_{c_1} \times N_f)}^{c_1 f} q_{(N_f \times 1)}^f. \quad (4.1.6)$$

Likewise, the equation for coarsening level 2 is written as:

$$\mathbf{R}_{(N_{c_2} \times N_{c_1})}^{c_2 c_1} A_{(N_{c_1} \times N_{c_1})}^{c_1} \left[\mathbf{P}_{(N_{c_1} \times N_{c_2})}^{c_1 c_2} p_{(N_{c_2} \times 1)}^{c_2} \right] = \mathbf{R}_{(N_{c_2} \times N_{c_1})}^{c_2 c_1} q_{(N_{c_1} \times 1)}^{c_1}. \quad (4.1.7)$$

In the equations above, $\mathbf{R}^{c_2 c_1}$ is the restriction operator which maps the first-level coarse scale to the second-level coarse scale, whereas $\mathbf{P}^{c_1 c_2}$ maps the second-level coarse scale to the first-level one.

It was shown in section 3.3.1 that $\mathbf{R}^c A^f \mathbf{P}^c = A^c$ and $\mathbf{R}^c q^f = q^c$. Therefore we can combine both Eqs. (4.1.6) and (4.1.7) to obtain MLMS equation in matrix-vector form as

$$\begin{aligned} \mathbf{R}^{c_2 c_1} \left(\mathbf{R}^{c_1 f} A^f \mathbf{P}^{f c_1} \right) \left[\mathbf{P}^{c_1 c_2} p^{c_2} \right] &= \mathbf{R}^{c_2 c_1} \left(\mathbf{R}^{c_1 f} q^f \right) \\ \Rightarrow \mathbf{R}^{c_2 c_1} \mathbf{R}^{c_1 f} A^f \mathbf{P}^{f c_1} \mathbf{P}^{c_1 c_2} p^{c_2} &= \mathbf{R}^{c_2 c_1} \mathbf{R}^{c_1 f} q^f. \end{aligned} \quad (4.1.8)$$

This equation can be written in an extended version. Assuming n level of coarsening, the MLMS equation in matrix-vector form can be written as

$$\mathbf{R} A^f \mathbf{P} p^{c_n} = \mathbf{R} q^f, \quad (4.1.9)$$

where

$$\mathbf{R} = \mathbf{R}^{c_n c_{n-1}} \mathbf{R}^{c_{n-1} c_{n-2}} \dots \mathbf{R}^{c_2 c_1} \mathbf{R}^{c_1 f} \quad (4.1.10)$$

is the MLMS restriction operator, and

$$\mathbf{P} = \mathbf{P}^{f c_1} \mathbf{P}^{c_1 c_2} \dots \mathbf{P}^{c_{n-2} c_{n-1}} \mathbf{P}^{c_{n-1} c_n} \quad (4.1.11)$$

is the MLMS prolongation operator.

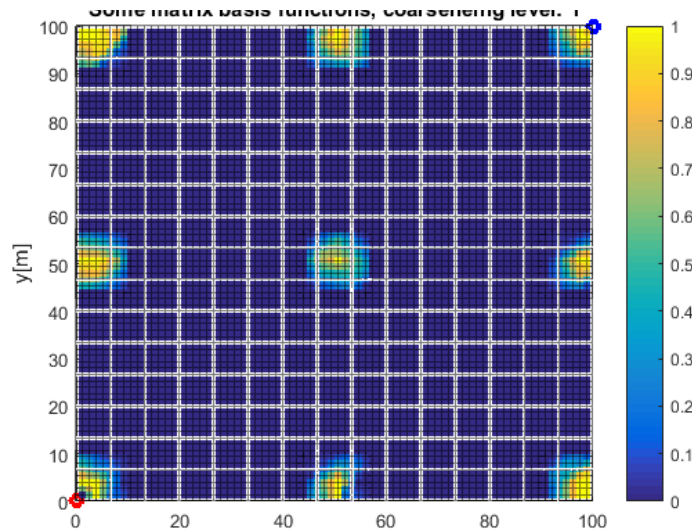
4.1.4. MLMS Basis Functions

Each coarsening level consists of independent basis functions. The number of basis functions in each level is equal to the number of coarse nodes at that specific level. The procedure to obtain the basis functions at each level is identical to MSFV method except for the fact that in second and higher levels the primal coarse cell of the previous coarse level is used as reference level of basis function construction on that coarser levels. Figures 4.2 and 4.3 show an example of basis functions for first and second coarsening level of the sample used previously in this chapter to demonstrate the coarse grid structure of MLMS (see fig. 4.1) with heterogeneity. Note that the basis function of the second coarsening level is plotted in a 15×15 matrix which shows how the primal coarse grids of the previous coarse level is used as an input in higher coarse level. The same procedure applies for the well function.

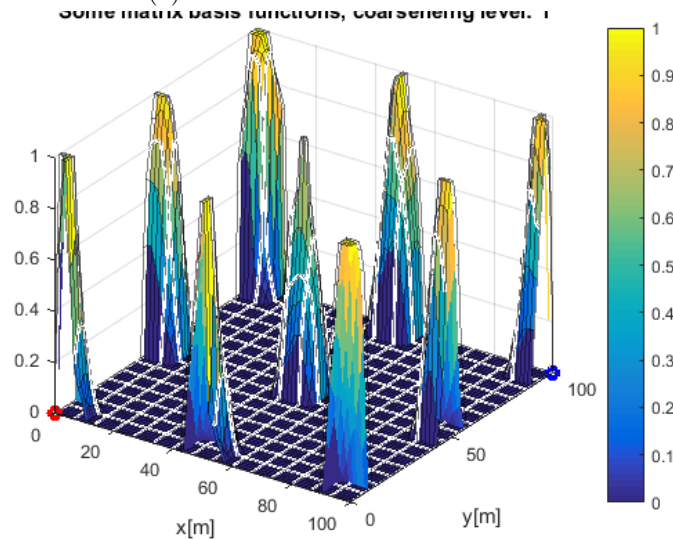
4.2. MultiLevel MultiScale Finite Volume Method for Fractured Porous Media” (F-MLMS)

4.2.1. F-MLMS Approach

In this section extension of MLMS into F-MLMS is explained and its implementation is described. MLMS provides higher efficiency for solving the system of equations with large amount of DOFs. Now it is important to apply the same technique for fractured porous media.



(a) Some basis functions in 2D view



(b) Some basis functions in 3D view

Figure 4.2: Some of the basis functions of the sample used in fig. 4.1, 75×75 with coarsening ratio of 5. These basis functions belong to the coarse level 1.

4.2.2. F-MLMS Implementation

The same procedure as in the F-MSFV (i.e., 1 level coarsening with fractures) is being followed, but now extended to multilevel resolutions. More precisely, the prolongation operators are constructed by clustering the basis functions at each coarsening level. At each level, prolongation operator is constructed using the explained Frac-AMS coupling method ($\mathcal{P}_{mf} = 0$ and $\mathcal{P}_{fm} \neq 0$).

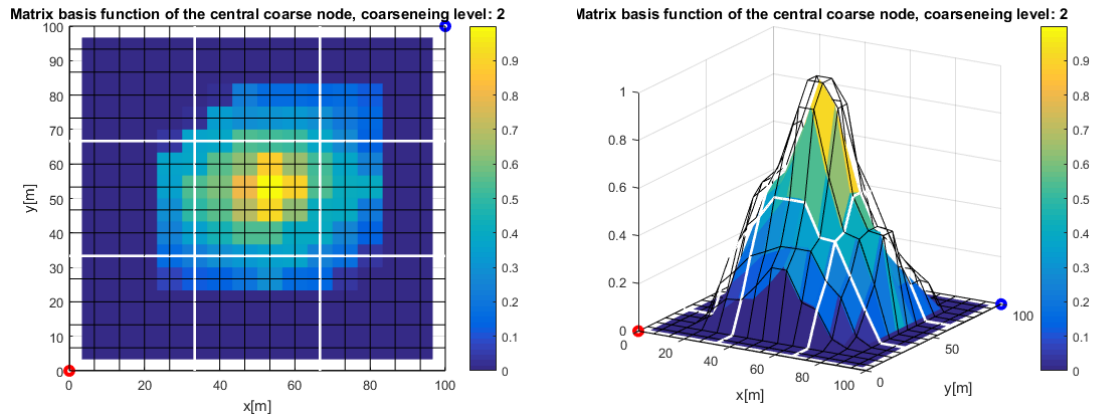


Figure 4.3: The basis function in the central coarse node of the sample used in fig. 4.1, 75×75 with coarsening ratio of 5. This basis function belongs to the coarse level 2. Basis function is shown in 2D (left) and 3D (right) views.

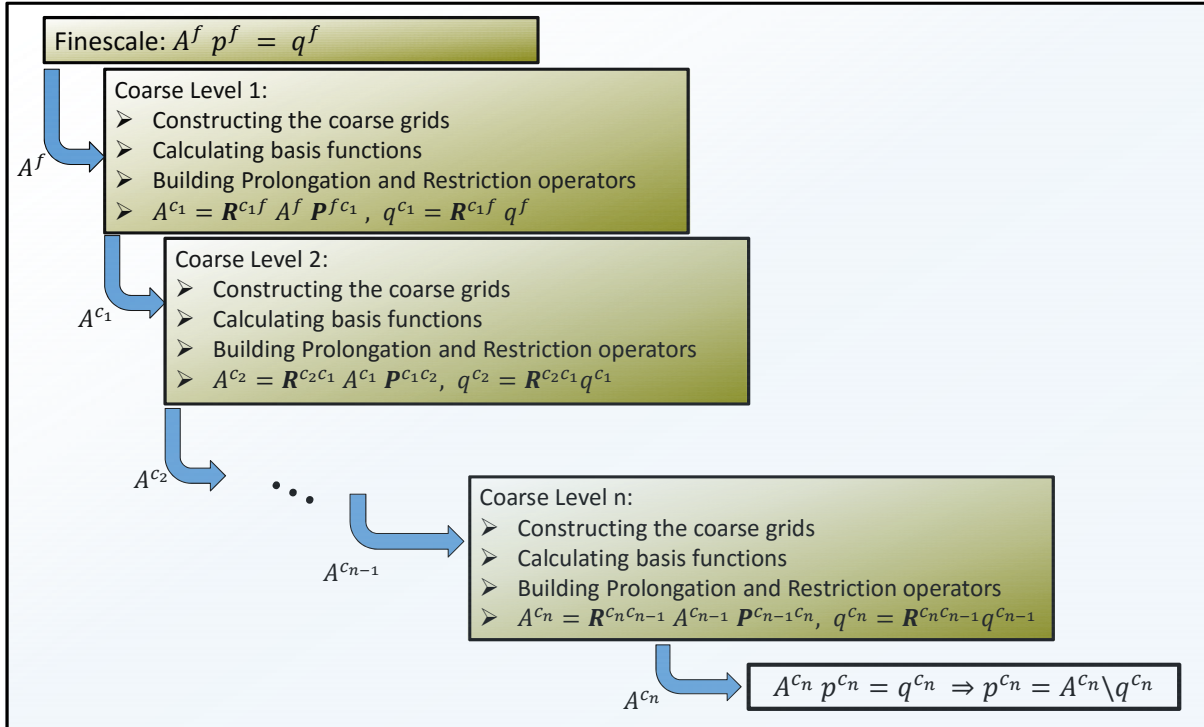


Figure 4.4: F-MLMS strategy to obtain solution at coarsest level.

4.2.3. F-MLMS Basis Functions

Matrix and well basis functions are calculated as it was mentioned in MLMS implementation except for the fact that the influence of fractures should be captured by adding Dirichlet boundary conditions at fracture elements (value of 0.0). Basis functions for fractures first need to be obtained by defining an support region around the fracture dual coarse cell. This is obtained based on the position of the mentioned fracture dual coarse cell in the matrix dual coarse cells. Before obtaining the fracture basis function, a 1D linear solution is calculated inside the fracture. Thereafter, the 1D solution is used as Dirichlet boundary condition for fracture basis function inside the matrix formation. The Frac-AMS coupling will be followed in all levels.

Computation of basis functions at first coarsening level uses tow-point flux approximation (TPFA) fine-scale system, meaning that each fine-scale matrix cell has connectivity with maximum four neighboring matrix grid cells (and of course with overlapping fracture elements). The edge cells are only connected to the neighboring interiors and edges. Vertexes are only connected to the neighboring edges and interiors have connectivity with neighboring edges and interiors (so no vertexes). Now, the coarse grid system of the first coarsening is seen as a fine grid system for next coarsening level. The coarse system is considered as multi-point flux approximation (MPFA) system (since all 8 neighbors of a cell have non-zero basis function inside its control volume). This means that each dual coarse block has connectivity not only by the neighboring blocks that have direct connection (left, bottom, right and top), but also with its diagonal neighbors [36]. Such implementation results in more accurate system, as it ensures a richer flux calculation between the dual blocks. The basis functions for second coarsening level are computed using MPFA defined naturally by the prior-level MSFV coarse system. The MPFA coarse system is again used for higher coarsening levels as well. Figure 4.5 represents the schematic view of TPFA and MPFA systems.

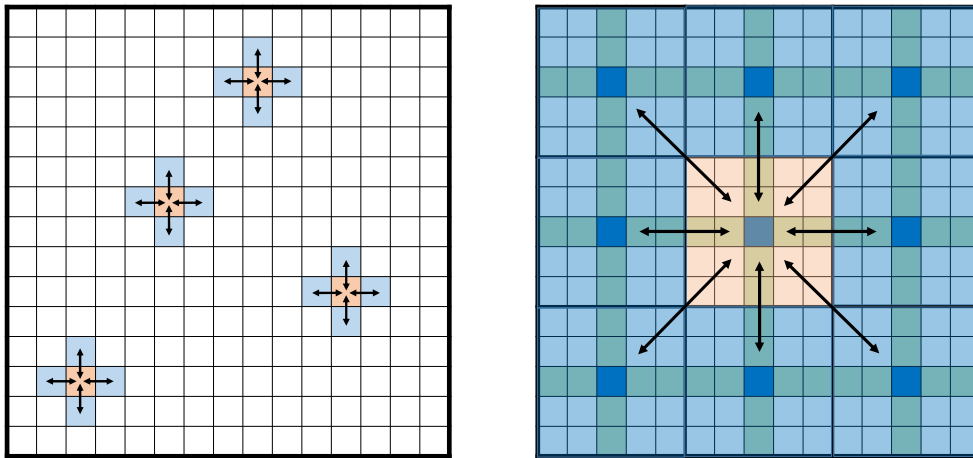
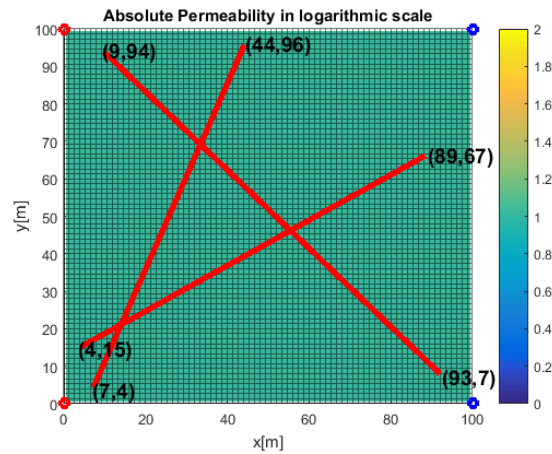
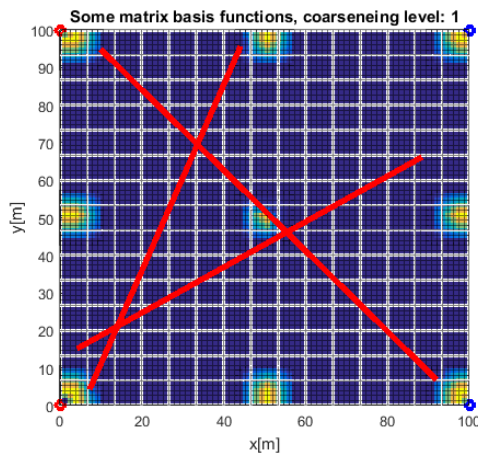


Figure 4.5: The two-point flux approximation (TPFA) fine system (left) considers connectivity of each fine-scale grid cell with only four direct neighbors whereas the multi-point flux approximation (MPFA) coarse system (right) accommodates the connectivity of each dual coarse with its diagonal neighbors as well. Computation of basis function for the first coarsening level uses TPFA fine system. For higher coarsening levels, MPFA coarse system is applied to obtain the basis functions.

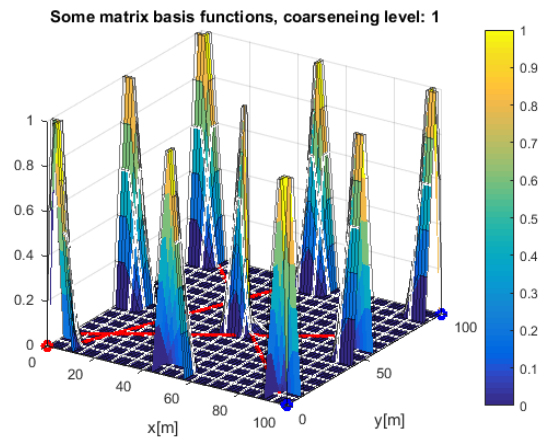
As a demonstration of basis functions in F-MLMS, let us assume an example of fractured porous media of homogeneous matrix with 75 cells and 3 fractures with total number of 228 elements. Figures 4.6 and 4.7 show some matrix and fracture basis functions for two coarsening levels (coarsening ratio is 5), respectively.



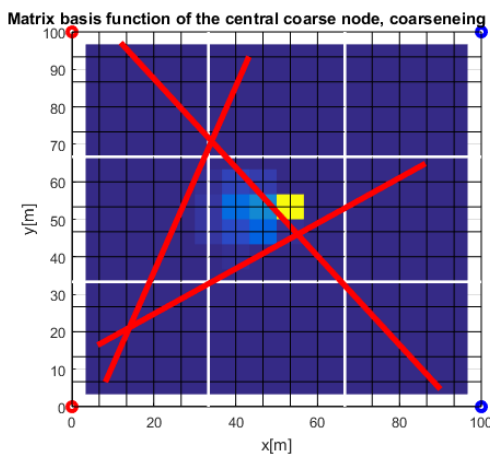
(a) Permeability of the matrix



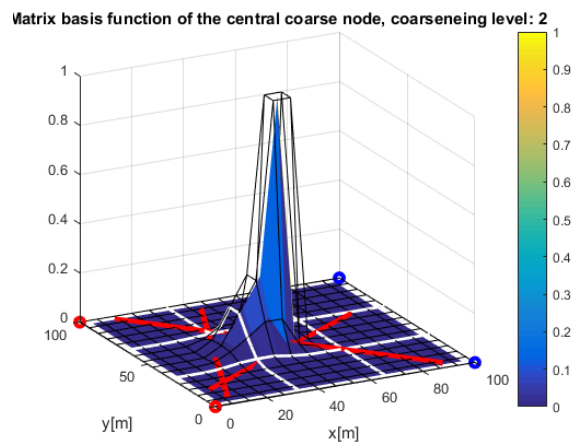
(b) Some matrix basis functions at coarsening level 1 in 2D view.



(c) Some matrix basis functions at coarsening level 1 in 3D view.

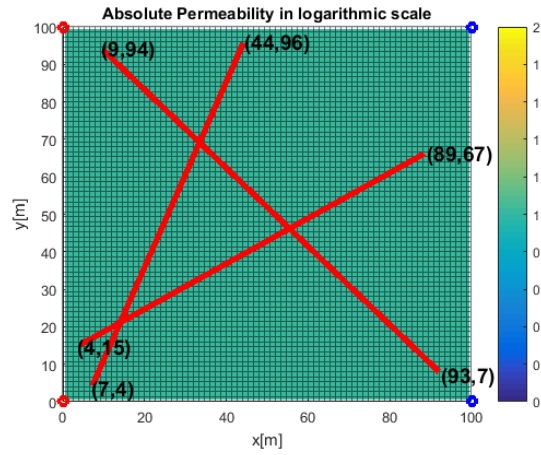


(d) The central matrix basis function at coarsening level 1 in 2D view.

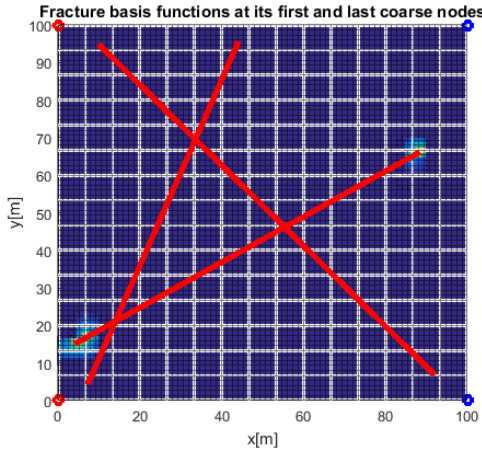


(e) The central matrix basis function at coarsening level 1 in 3D view.

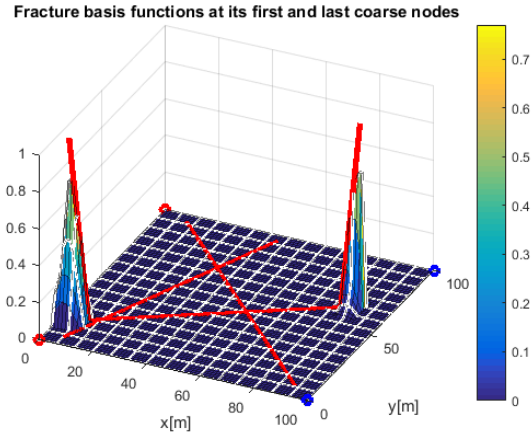
Figure 4.6: Some matrix basis functions at coarsening level 1 (b,c) and the central matrix basis function at coarsening level 2 (d,e).



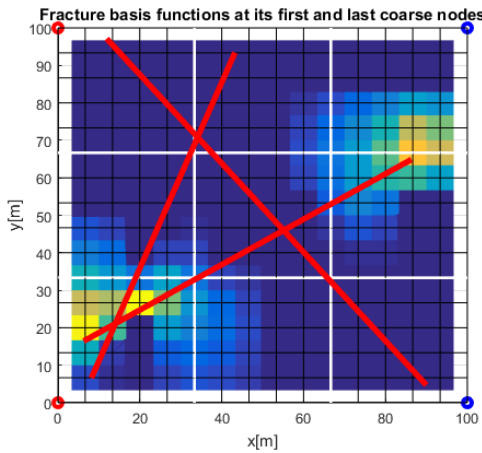
(a) Permeability of the matrix



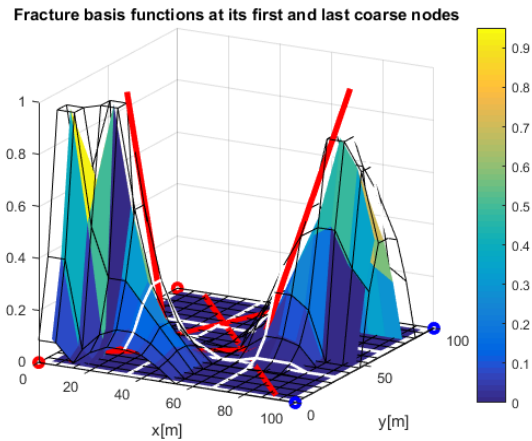
(b) First and last basis functions of one of the fractures at coarsening level 1 in 2D view.



(c) First and last basis functions of one of the fractures at coarsening level 1 in 3D view.



(d) First and last basis functions of one of the fractures at coarsening level 2 in 2D view.



(e) First and last basis functions of one of the fractures at coarsening level 2 in 3D view.

Figure 4.7: First and last basis functions of one of the fractures at coarsening level 1 (b,c) and coarsening level 2 (d,e).

Chapter 5

MLMS and F-MLMS Results and Discussion

In this chapter results from MLMS and F-MLMS are presented. Different test cases are designed to address various possible challenges. The sensitivity of the MLMS and the F-MLMS methods to the number of coarse levels and the coarsening ratios employed and to the permeability contrast is presented.

The second-norm of the pressure error is calculated for all results the same as in previous sections:

$$Err_{norm} = \frac{\|p_{ms} - pfs\|_2}{\|pfs\|_2} \quad (3.5.1)$$

Where, $\|p_{ms} - pfs\|_2 = \sqrt{\sum_{i=1}^{N_f} [p_{ms_i} - pfs_i]^2}$, and $\|pfs\|_2 = \sqrt{\sum_{i=1}^{N_f} [pfs_i]^2}$.

p_{ms_i} and pfs_i are the finescale and (approximated) multiscale pressure solutions at cell i (either in the matrix or the fractures) respectively.

5.1. Test Case 1: MLMS Line Drive (Four Spot)

This test case contains 81×81 homogeneous sample with two injection wells at left corners and two production wells at right corners. The coarsening level is 3 and coarsening ratio is 3 as well. See figure 5.1 for results.

5.2. Test Case 2: MLMS Quarter of Five Spot

This test case is a 100×100 heterogeneous sample with quarter of five spot well pattern (one injection well at bottom left corner and one production well at top right corner). The coarsening level is 2 and coarsening ratio is 5. The permeability contrast is $k_{max}/k_{min} = 1.24 \times 10^4$. Figure 5.2 shows the result of this test case.

5.3. Test Case 3: F-MLMS Quarter of Five Spot with One Diagonal Fracture

Test case 3, where one diagonal fracture lies in a homogeneous matrix with one injection well at bottom left corner and one production well at top right corner. Test case consists of $135 \times 135 = 18225$ matrix cells and 82 fracture elements. The coarsening level is 3 and coarsening ratio is 3. Figure 5.3 contains the results for this test case.

5.4. Test Case 4: F-MLMS Line Drive with Two Fractures Perpendicular to each other, ”+” Shape

in test case 4, Two Fractures Perpendicular to each other, as ”+” Shape, exist in a heterogeneous matrix with line drive of five injection wells at left boundary and five production wells at the right boundary. Test case consists of $100 \times 100 = 10000$ matrix cells and 152 fracture elements. The coarsening level is 2 and coarsening ratio is 5. Figure 5.4 contains the results for this test case.

5.5. Test Case 5: F-MLMS Line Drive with 5 Random Fractures Intersecting with Each Other

This test case (5), has five random fractures intersecting with each other in a homogeneous matrix with line drive of five injection wells at left boundary and five production wells at the right boundary. Test case consists of $75 \times 75 = 5625$ matrix cells and 380 fracture elements. The coarsening level is 2 and coarsening ratio is 5. Figure 5.5 contains the results for this test case.

5.6. Test Case 6: Comparison: F-MLMS Line Drive with Two Diagonal Fractures Perpendicular to Each Other, ”x” shape

In this test case, two diagonal fractures in the center perpendicular to each other, are present in a homogeneous matrix with line drive of five injectors and 5 producers. The sample has 81×81 matrix cells and 164 fracture elements. Solution sensitivity and error analysis will be studied for different coarsening levels and coarsening ratios in this sample. The following options will be considered:

1. Finescale (reference) solution
2. One level coarsening, coarsening ratio = 3
3. One level coarsening, coarsening ratio = 9
4. One level coarsening, coarsening ratio = 27
5. Two level coarsening, coarsening ratio = 3
6. Three level coarsening, coarsening ratio = 3

Figure 5.6 shows the permeability map of this test case. Results are shown in figure 5.7. Note that the errors mentioned in the figure are second norm errors calculated by equation (3.5.1).

5.7. Discussion and Validation of Results

The accuracy of the MLMS is being verified for several test cases. As can be seen, the residual is non-zero only at the boundaries of the dual-coarse cells, due to the localization assumption. Note that the presented results are all based on the MLMS procedure, despite the fact that an iterative procedure could have been employed to improve them. This ensures the original (non-iterative) multilevel multiscale, proposed in this work, is quite accurate to capture the complex effects of fractures, rock heterogeneity, and wells into arbitrary levels of coarse grids. For test cases with high-permeability contrasts and strong anisotropic permeability tensors, though, one needs to consider iterative procedure to ensure the quality of the results. Important to emphasize here is that Test Case 6 compares the results of fine-scale solution to five different multiscale and multilevel multiscale solutions. As it can be seen, multilevel multiscale method provides more

accurate solutions compared to one-level multiscale solutions. Figure 5.7c shows results of 1 level multiscale with coarsening ratio of 9 and figure 5.7d shows the results of 2 level multiscale with coarsening ratio of 3 (corresponding to the same final coarse-scale resolution). Both solutions are obtained with 9×9 coarse grid cells. The multilevel multiscale (Fig. 5.7d) has smaller error thus being more accurate. The same holds for 3 level multiscale. Figure 5.7e shows results of 1 level multiscale with coarsening ratio of 27 and figure 5.7f shows the results of 3 level multiscale with coarsening ratio of 3. Both solutions are obtained with 3×3 coarse grid cells and the 3 level multiscale solution is more accurate than the 1 level multiscale solution. Note that the accuracy of both F-MLMS (many coarse levels) and F-MSFV (1 coarse level) depends on the quality of the localization assumptions, and no concrete conclusion on the accuracy of each method can be made with these results. Important is that through iterative procedure, one can always guarantee the quality of any multiscale solution. And, the F-MLMS is much more efficient than F-MSFV. All at the end, F-MLMS is found to be a significant step forward in the development of real-field multiscale procedures. Finally, F-MLMS automatically reduced to F-MSFV if only 1 level of coarse grid is employed. This gives full flexibility to the client, when real-field applications are being studied.

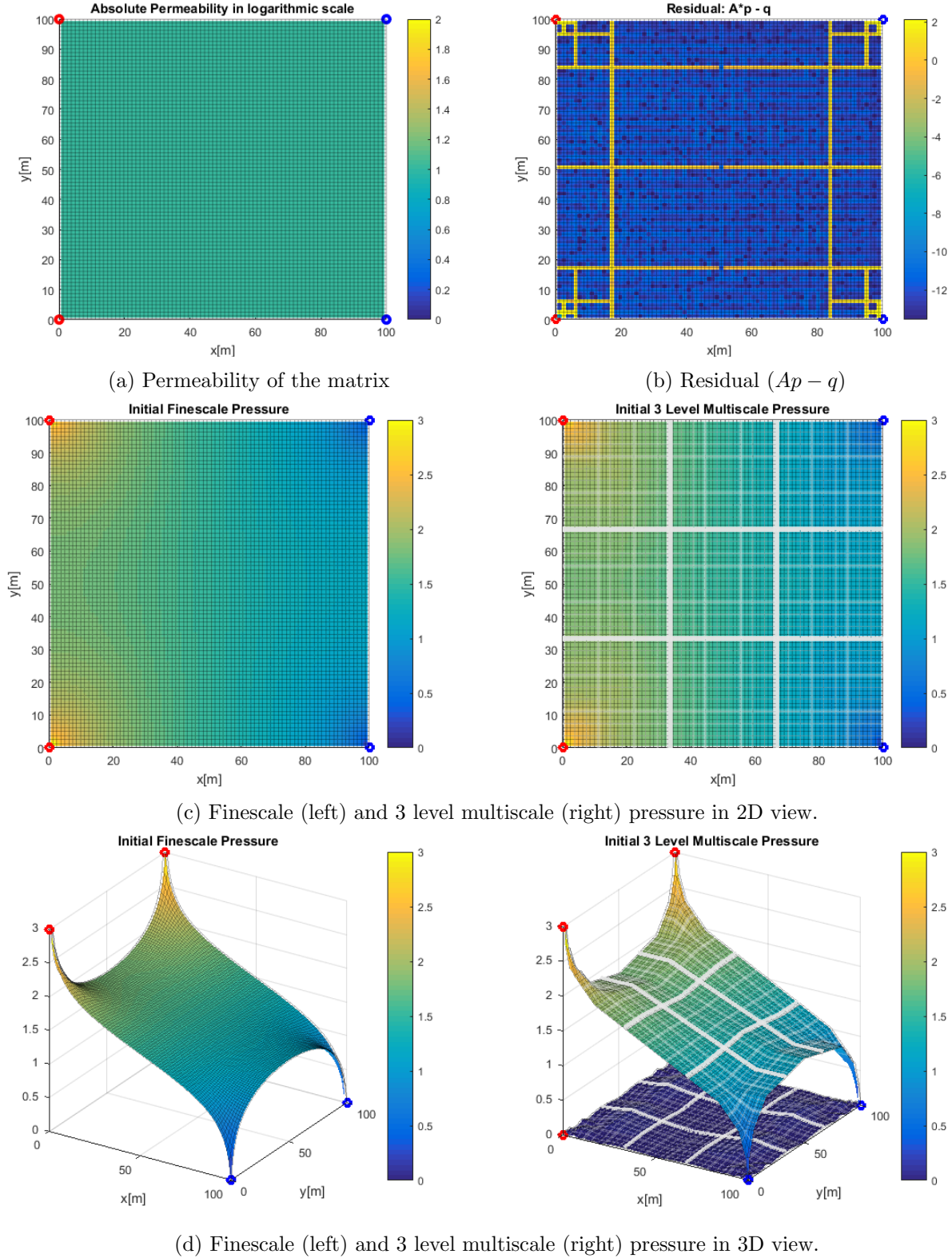


Figure 5.1: Results of test case 1: a) homogeneous permeability plot in logarithmic scale with well positioning. b) residual ($Ap - q$) plot in logarithmic scale indicating non-zero values at dual coarse cell boundaries. c,d) pressure solution in 2D and 3D views. The graphs at left show the finescale pressure result (solved with 81×81 cells) where the graphs at right show MLMS pressure result (solved by 3×3 coarse cells) with significantly less number of DOFs. The coarsening level is 3 and the coarsening ratio is 3. The white lines indicate the boundaries of primal coarse grids. The plotted graph below the 3D MLMS graph in the right figure is the difference between finescale and MLMS solution. The normalized error is $\frac{\|p_{ms} - p_{fs}\|_2}{\|p_{fs}\|_2} = 2.71 \times 10^{-2}$.

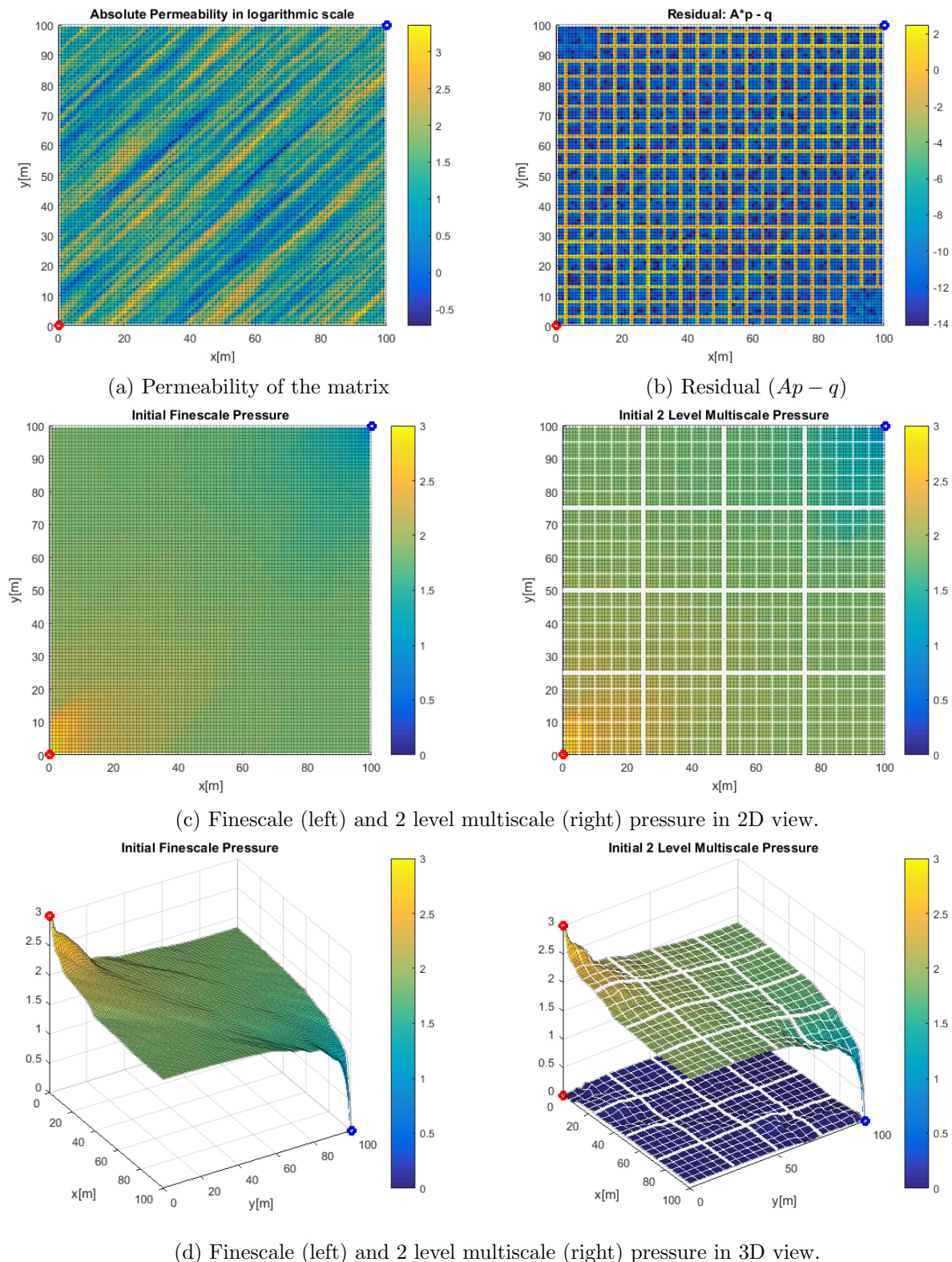


Figure 5.2: Results of test case 2: a) heterogeneous permeability plot in logarithmic scale with well positioning. b) residual ($Ap - q$) plot in logarithmic scale indicating non-zero values at dual coarse cell boundaries. c,d) pressure solution in 2D and 3D views. The graphs at left show the finescale pressure result (solved with 100×100 cells) where the graphs at right show MLMS pressure result (solved by 4×4 coarse cells) with significantly less number of DOFs. The coarsening level is 2 and the coarsening ratio is 5. The white lines indicate the boundaries of primal coarse grids. The plotted graph below the 3D MLMS graph in the right figure is the difference between finescale and MLMS solution. The normalized error is $\frac{\|p_{ms} - p_{fs}\|_2}{\|p_{fs}\|_2} = 3.27 \times 10^{-2}$.

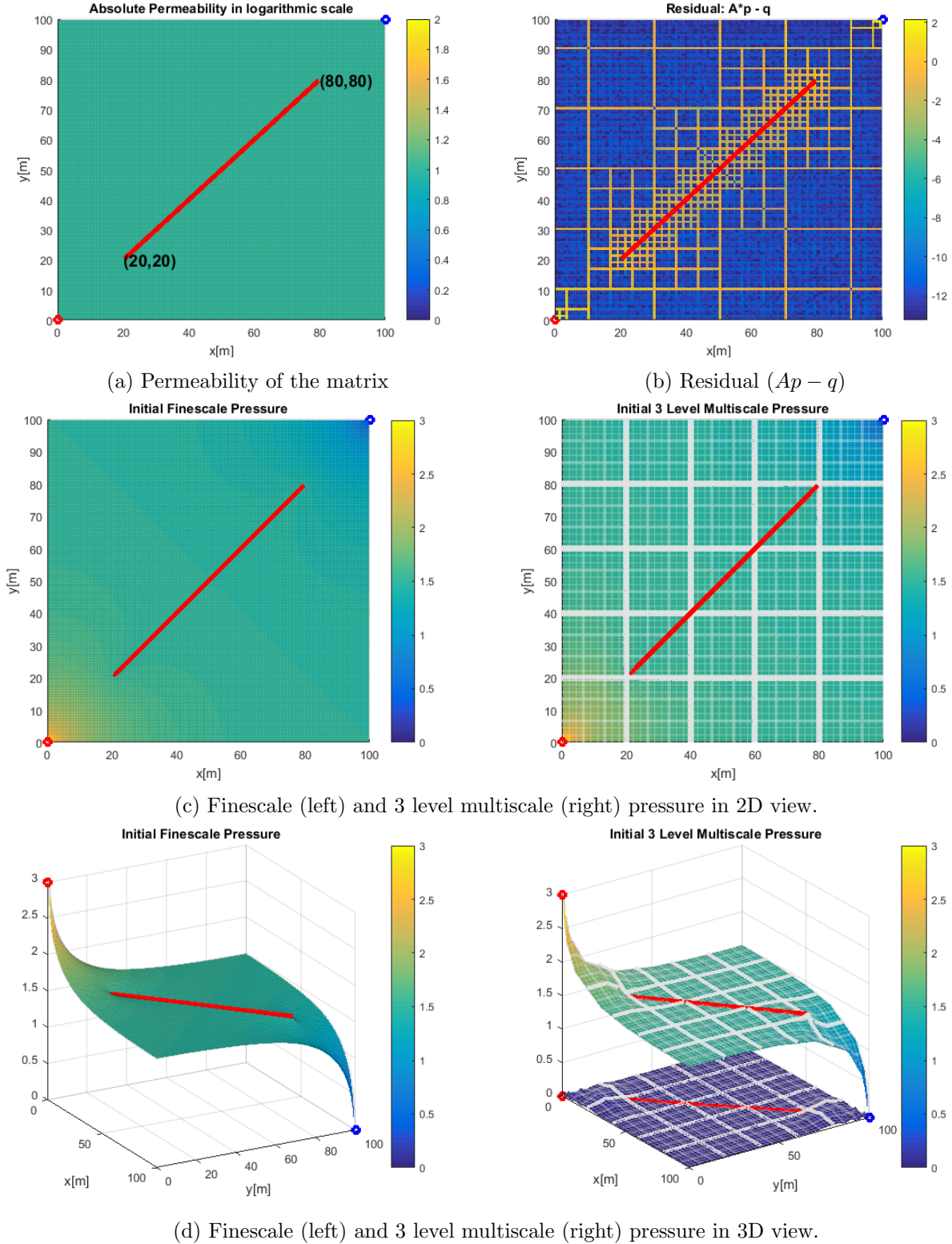


Figure 5.3: Results of test case 3: a) homogeneous permeability plot in logarithmic scale with fracture and well positioning. b) residual ($Ap - q$) plot in logarithmic scale indicating non-zero values at dual coarse cell boundaries. c,d) pressure solution in 2D and 3D views. The graphs at left show the finescale pressure result (solved with 135×135 matrix cells and 82 fracture elements) where the graphs at right show MLMS pressure result (solved by 5×5 matrix coarse cells and 4 fracture course cells) with significantly less number of DOFs. The coarsening level is 3 and the coarsening ratio is 3. The white/grey lines indicate the boundaries of primal coarse grids. The plotted graph below the 3D MLMS graph in the right figure is the difference between finescale and MLMS solution. The normalized error is $\frac{\|p_{m.s} - p_{f.s}\|_2}{\|p_{f.s}\|_2} = 1.16 \times 10^{-2}$.

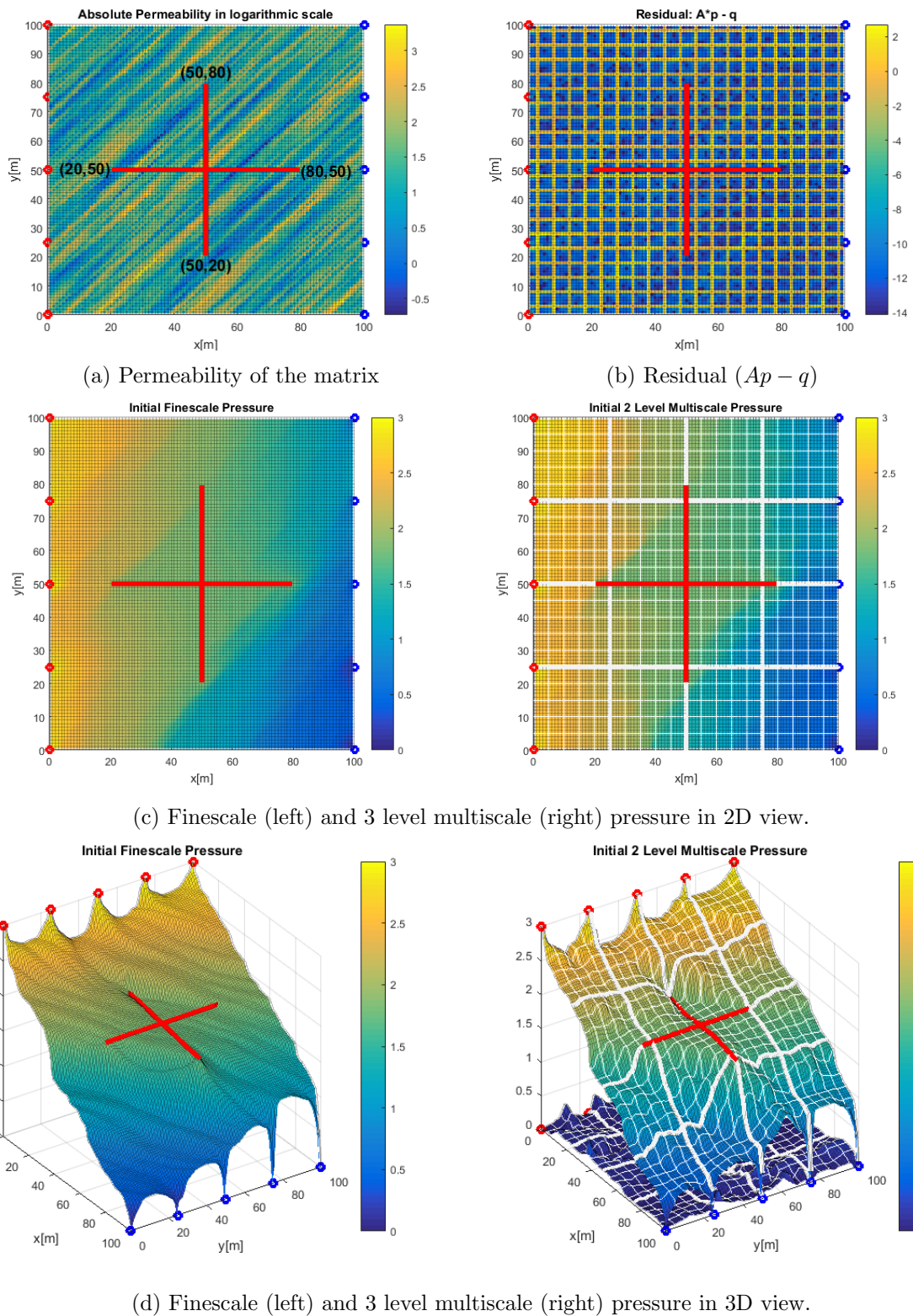


Figure 5.4: Results of test case 4: a) heterogeneous permeability plot in logarithmic scale with fractures and well positioning. b) residual ($Ap - q$) plot in logarithmic scale indicating non-zero values at dual coarse cell boundaries. c,d) pressure solution in 2D and 3D views. The graphs at left show the finescale pressure result (solved with 100×100 matrix cells and 152 fracture elements) where the graphs at right show F-MLMS pressure result (solved by 4×4 matrix coarse cells and 8 fracture course cells) with significantly less number of DOFs. The coarsening level is 2 and the coarsening ratio is 5. The white/grey lines indicate the boundaries of primal coarse grids. The plotted graph below the 3D MLMS graph in the right figure is the difference between finescale and MLMS solution. The normalized error is $\frac{\|p_{ms} - p_{fs}\|_2}{\|p_{fs}\|_2} = 4.40 \times 10^{-2}$.

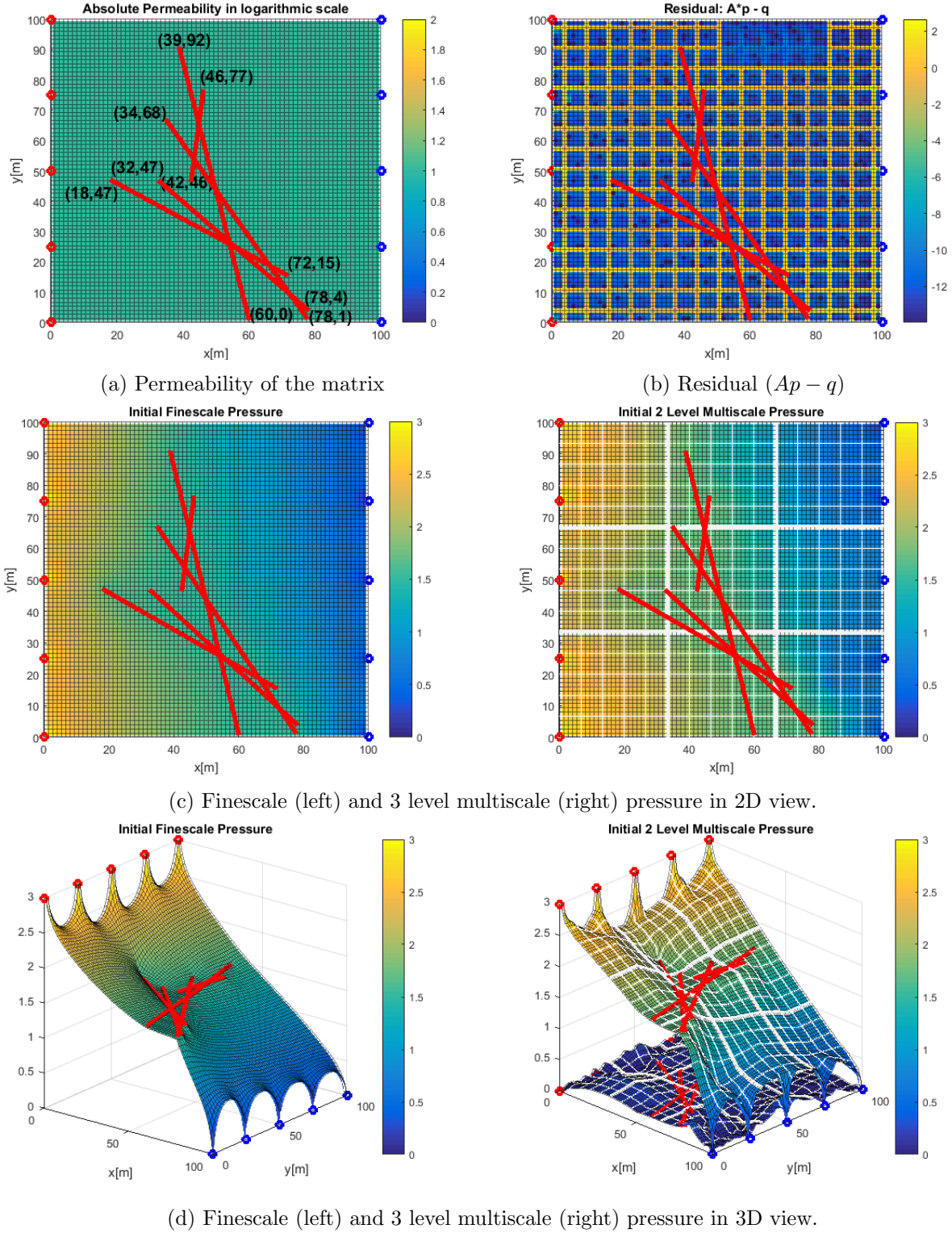


Figure 5.5: Results of test case 5: a) homogeneous permeability plot in logarithmic scale with fractures and well positioning. b) residual ($Ap - q$) plot in logarithmic scale indicating non-zero values at dual coarse cell boundaries. c,d) pressure solution in 2D and 3D views. The graphs at left show the finescale pressure result (solved with 75×75 matrix cells and 380 fracture elements) where the graphs at right show F-MLMS pressure result (solved by 3×3 matrix coarse cells and 20 fracture course cells) with significantly less number of DOFs. The coarsening level is 2 and the coarsening ratio is 5. The white/grey lines indicate the boundaries of primal coarse grids. The plotted graph below the 3D MLMS graph in the right figure is the difference between finescale and MLMS solution. The normalized error is $\frac{\|p_{ms} - p_{fs}\|_2}{\|p_{fs}\|_2} = 7.85 \times 10^{-2}$.

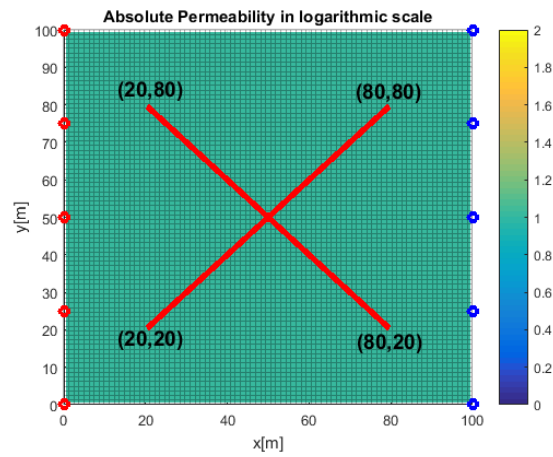


Figure 5.6: Test case 6: homogeneous permeability plot in logarithmic scale with fractures and well positioning. The sample has 81×81 matrix cells and 164 fracture elements.

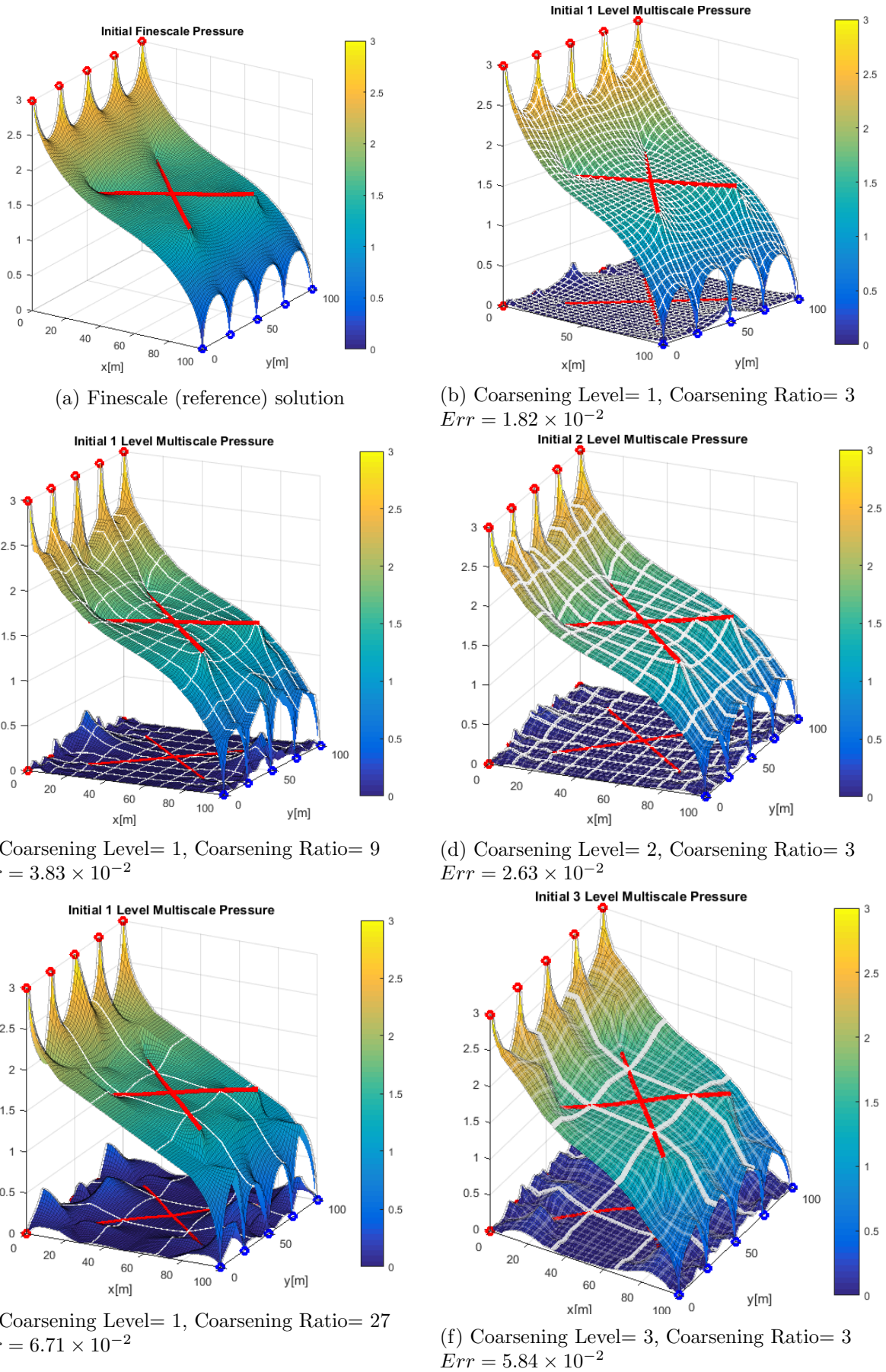


Figure 5.7: Test case 6: Pressure solution with different coarsening levels ratios. The second norm error is calculated by equation (3.5.1).

Chapter 6

Conclusion

The large scale of the natural reservoirs together with high heterogeneity and presence of complex fracture networks (which requests very high resolutions to capture the thin beds of fractures) result in multi-billion cell problems. Solving such problems (with so many unknowns and DOFs) makes it impossible for simulators to use conventional numerical methods. One may suggest up-scaling to reduce the number of unknowns by averaging the heterogeneity quantities of matrix and fractures together. However, upscaling causes huge amount of information loss and high in-accuracy. EDFM (see section 2) provides a better solution by discretizing fractures independently from matrix which fades the necessity of very high resolution as fractures are treated in a separate computational system. Yet, the huge number of grid cells prevents the practical application of this method to provide solution for real-field applications. Therefore MSFV and F-MSFV (chapter 3) were introduced by solving the problem in a coarser scale but without loss of information or up-scaling. They provide acceptable approximation of fine-scale solution, yet allowing for systematic error reduction if an iterative multiscale strategy is followed. Without any iterative procedure to improve the multiscale accuracy, MSFV is sensitive to high heterogeneity contrasts.

F-MSFV however is still not fully capable of treating a real scale problem with billions of grid cells. Therefore, multiscale concept has been extended to include multiple levels of coarsening. Multilevel multiscale (MLMS) allows for coarsening into coarser domains (with fewer grid cells) one after another, obtaining the coarse solution at the coarsest level and mapping into finer scale and at the end providing an acceptable approximation to fine-scale solution (see section 4). In this work, F-MLMS was devised to allow for application of multilevel multiscale for fractured porous media gathering the benefits of EDFM and multilevel multiscale all in one method. Multiple coarsening for matrix and fractures helps us to turn a multi-billion cells problem with complex fracture networks into a problem with million grid cells or even less, allowing us to solve real scale field problems with much higher efficiency and less computational costs. In the future, one can apply this method to Algebraic Dynamic Multilevel multiscale solver (ADM) having a robust and advanced numerical solver to extend our capability to solve problems with even larger scales and more DOFs (ADM dynamically sets the level of coarsening at each location of the media based on the error criterion [37]).

Bibliography

- [1] M. Tene, M. S. Al Kobaisi, and H. Hajibeygi. Algebraic multiscale method for flow in heterogeneous porous media with embedded discrete fractures (f-ams). *Journal of Computational Physics*, 321(1):819–845, 2016.
- [2] Karimi-Fard, L.J. Durlofsky, and K.Aziz. An efficient discrete-fracture model applicable for general-purpose reservoir simulators. *SPE Journal*, pages 227–236, June 2004.
- [3] B. Berkowitz. Characterizing flow and transport in fractured geological media: A review. *Advances in Water Resources*, 25:861–884, 2002.
- [4] J.E. Warren and P.J. Root. The behavior of naturally fractured reservoirs. *SPE Journal*, 3(SPE-426-PA):245–255, 1963.
- [5] G.I. Barenblatt, Iu.P. Zheltov, and I.M. Kochina. Basic concepts in the theory of seepage of homogeneous liquids in fissured rocks. *PMM*, 24(5):852–864, 1960.
- [6] H. Kazemi, L.S. Merrill, K.L. Porterfield, and P.R. Zeman. Numerical simulation of water-oil flow in naturally fractured reservoirs. *SPE Journal*, (5719):317–326, December 1996.
- [7] P. Dietrich, R. Helmig, M. Sauter, H. Hotzl, J. Kongeter, and G. Teutsch. *Flow and Transport in Fractured Porous Media*. Springer, 2005.
- [8] C. L. Jensen S. H. Lee and M. F. Lough. An efficient finite difference model for flow in a reservoir with multiple length-scale fractures. *SPE ATCE*, October 1999.
- [9] S.H. Lee, M.F. Lough, and C.L. Jensen. Hierarchical modeling of flow in naturally fractured formations with multiple length scales. *Water Resource Research*, 37(3):443–455, March 2001.
- [10] H. Hajibeygi, D. Karvounis, and P. Jenny. An upstream finite element method for solution of transient transport equation in fractured porous media. *Journal of Computational Physics*, 230:8729–8743, 2012.
- [11] L. Li and S. H. Lee. Efficient field-scale simulation of black oil in naturally fractured reservoir through discrete fracture networks and homogenized media. *SPE Reservoir Evaluation and Engineering*, pages 750–758, 2008.
- [12] R Ahmed, Michael G Edwards, Sadok Lamine, B A H Huisman, and M Pal. Control-volume distributed multi-point flux approximation coupled with a lower-dimensional fracture model. *J. Comput. Phys.*, 284:462–489, 2015.
- [13] D. C. Karvounis. *Simulations of Enhanced Geothermal Systems with an Adaptive Hierarchical Fracture Representation*. PhD thesis, ETH Zurich, 2013.
- [14] V. Reichenberger, H. Jakobs, P. Bastian, and Rainer Helmig. A mixed-dimensional finite volume method for two-phase flow in fractured porous media. *Advances in Water Resources*, 29:1020–1036, 2006.

- [15] A. Moinfar, A. Varavei, K. Sepehrnoori, and R. T. Johns. Development of an efficient embedded discrete fracture model for 3d compositional reservoir simulation in fractured reservoirs. *SPE J.*, 19:289–303, 2014.
- [16] S.B. Plumiers. Hierarchical fracture modeling approach. Msc thesis, TU Delft, 2015.
- [17] H. Hajibeygi, D. Karvounis, and P. Jenny. A hierarchical fracture model for the iterative multiscale finite volume method. *Journal of Computational Physics*, 230(24):8729 – 8743, 2011.
- [18] M. Tene, M. S. Al Kobaisi, and H. Hajibeygi. Multiscale projection-based embedded discrete fracture modeling approach (f-ams-pedfm). In *ECMOR XV-15th European conference on the mathematics of oil recovery*, 2016.
- [19] Yixuan Wang, Hadi Hajibeygi, and Hamdi A. Tchelepi. Algebraic multiscale solver for flow in heterogeneous porous media. *Journal of Computational Physics*, 259:284 – 303, 2014.
- [20] H. Hajibeygi, G. Bonfigli, M.A. Hesse, and P. Jenny. Iterative multiscale finite-volume method. *J. Comput. Phys.*, 227:8604–8621, 2008.
- [21] H. Hajibeygi, S. H. Lee, and I. Lunati. Accurate and efficient simulation of multiphase flow in a heterogeneous reservoir by using error estimate and control in the multiscale finite-volume framework. *SPE J.*, 17(4):1071–1083, 2012.
- [22] P Jenny, S.H Lee, and H.A Tchelepi. Multi-scale finite-volume method for elliptic problems in subsurface flow simulation. *Journal of Computational Physics*, 187(1):47 – 67, 2003.
- [23] T. Y. Hou and X.-H. Wu. A multiscale finite element method for elliptic problems in composite materials and porous media. *J. Comput. Phys.*, 134:169–189, 1997.
- [24] Y. Efendiev, T. Hou, and V. Ginting. Multiscale finite element methods for nonlinear problems and their applications. *COMM. MATH. SCI.*, 2:553–589, 2004.
- [25] Y. Efendiev, V. Ginting, T. Hou, and R. Ewing. Convergence of a nonconforming multiscale finite element method. *SIAM J. NUMER. ANAL.*, 37:888–910, 2000.
- [26] H. Hajibeygi and H. A. Tchelepi. Compositional multiscale finite-volume formulation. *SPE J.*, 19:316–326, 2014.
- [27] Y. Wang, H. Hajibeygi, and H. A. Tchelepi. Monotone multiscale finite volume method. *Comput. Geosci.*, 20:509–524, 2016.
- [28] M. Tene, Y. Wang, and H. Hajibeygi. Adaptive algebraic multiscale solver for compressible flow in heterogeneous porous media. *J. Comput. Phys.*, 300:679–694, 2015.
- [29] D. Cortinovis and Patrick Jenny. Iterative galerkin-enriched multiscale finite-volume method. *J. Comp. Phys.*, 277:248–267, 2014.
- [30] M. Cusini, A. Lukyanov, J. Natvig, and H. Hajibeygi. Constrained pressure residual multiscale (CPR-MS) method for fully implicit simulation of multiphase flow in porous media. *J. Comput. Phys.*, 299:472–486, 2015.
- [31] O. Moyner and K.A. Lie. A multiscale restriction-smoothed basis method for high contrast porous media represented on unstructured grids. *J. Comput. Phys.*, 304:46–71, 2016.
- [32] H. Hajibeygi, G. Bonfigli, M. A. Hesse, and P. Jenny. Iterative multiscale finite-volume method. *Journal of Computational Physics*, 227(19):8604 – 8621, 2008.

- [33] R. Kunze, I. Lunati, and S. H. Lee. A multilevel multiscale finite-volume method. *Journal of Computational Physics*, 255:502 – 520, 2013.
- [34] K. Aziz and A. Settari. *Petroleum Reservoir Simulation*. Blitzprint Ltd., Calgary, Alberta, 2002.
- [35] H. Hajibeygi. *Iterative multiscale finite-volume method for multiphase flow in porous media with complex physics*. Phd thesis, ETH Zurich, Switzerland, 2011.
- [36] I. Aavatsmark. An introduction to multipoint flux approximations for quadrilateral grids. *Computational Geosciences*, 6:405 – 432, 2002.
- [37] M. Cusini, C. van Kruijsdijk, and H. Hajibeygi. Algebraic dynamic multilevel (adm) method for fully implicit simulations of multiphase flow in porous media. *Journal of Computational Physics*, 314:60 – 79, 2016.